

---

# FourierMamba: Fourier Learning Integration with State Space Models for Image Deraining

---

Dong Li<sup>\*1</sup> Yidi Liu<sup>\*1</sup> Xueyang Fu<sup>1</sup> Jie Huang<sup>1</sup> Senyan Xu<sup>1</sup> Qi Zhu<sup>1</sup> Zheng-Jun Zha<sup>1</sup>

## Abstract

Image deraining aims to remove rain streaks from rainy images and restore clear backgrounds. Currently, some research that employs the Fourier transform has proved to be effective for image deraining, due to it acting as an effective frequency prior for capturing rain streaks. However, despite there exists dependency of low frequency and high frequency in images, these Fourier-based methods rarely exploit the correlation of different frequencies for conjuncting their learning procedures, limiting the full utilization of frequency information for image deraining. Alternatively, the recently emerged Mamba technique depicts its effectiveness and efficiency for modeling correlation in various domains (e.g., spatial, temporal), and we argue that introducing Mamba into its unexplored Fourier spaces to correlate different frequencies would help improve image deraining. This motivates us to propose a new framework termed FourierMamba, which performs image deraining with Mamba in the Fourier space. Owing to the unique arrangement of frequency orders in Fourier space, the core of FourierMamba lies in the scanning encoding of different frequencies, where the low-high frequency order formats exhibit differently in the spatial dimension (unarranged in axis) and channel dimension (arranged in axis). Therefore, we design FourierMamba that correlates Fourier space information in the spatial and channel dimensions with distinct designs. Specifically, in the spatial dimension Fourier space, we introduce the zigzag coding to scan the frequencies to rearrange the orders from low to high frequencies, thereby orderly correlating the connections between frequencies; in the channel dimension Fourier space with arranged

orders of frequencies in axis, we can directly use Mamba to perform frequency correlation and improve the channel information representation. Extensive experiments reveal that our method outperforms state-of-the-art methods both qualitatively and quantitatively.

## 1. Introduction

Images taken in rainy conditions exhibit significant degradation in detail and contrast due to rain in the air, leading to unpleasant visual results and the loss of frequency information. This issue can severely impact the performance of outdoor computer vision systems, such as autonomous driving and video surveillance (Wang et al., 2022a). To mitigate the effects of rain, many image deraining methods (Fu et al., 2011; Xiao et al., 2022) have emerged in recent years, aiming to remove rain streaks and restore clear backgrounds in images.

The advent of deep learning has spurred this field forward, with several learning-based deraining methods achieving remarkable success (Fu et al., 2017b; Yang et al., 2017; Zhang & Patel, 2018). Among them, some studies utilize the Fourier transform for deraining in the frequency domain (Zhou et al., 2023; Guo et al., 2022), proving effective. The key insights inspiring the use of the Fourier transform for image deraining are twofold: 1) The Fourier transform can separate image degradation and content components to some extent, serving as a prior for image deraining, as shown in Figure 1; 2) The Fourier domain possesses global properties, where each pixel in Fourier space is involved with all spatial pixels. Thus, it makes sense to explore the task of rain removal using the Fourier transform. However, despite the existence of low frequency and high frequency dependencies in images, previous Fourier-based methods rarely utilize the correlation of different frequencies to combine their learning process. As shown in Figure 1, the commonly used  $1 \times 1$  convolutions cannot correlate different frequencies, limiting the full utilization of frequency information in the image. Therefore, we seek to exploit the beneficial properties of the Fourier transform while exploring correlating different frequencies.

<sup>\*</sup>Equal contribution <sup>1</sup>University of Science and Technology of China, Hefei, China. Correspondence to: Zheng-Jun Zha <[zhazj@ustc.edu.cn](mailto:zhazj@ustc.edu.cn)>.

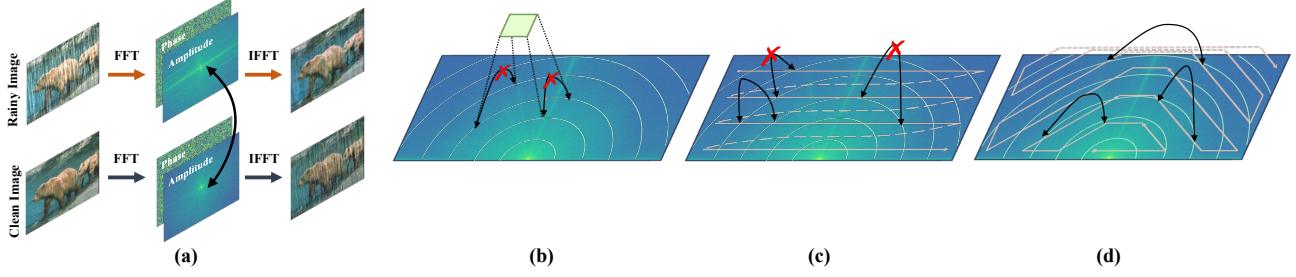


**Figure 1.** Observation and comparison of different frequency modeling methods. (a) Observation of the amplitude spectrum exchange. The degradation is mainly in amplitude components, so the Fourier transform helps to disentangle the image content and rain. (b) The commonly used  $1 \times 1$  convolution cannot model the relationship between different frequencies. (c) Previous scanning in Fourier space will fail to establish the ordered dependence between frequencies. (d) Our proposed method achieves ordered frequency dependence from low to high (or vice versa), thus fully utilizing frequency information.

Recently, an improved structured state-space sequence model (S4) with a selective scanning mechanism, Mamba, gives us hope. The selective methodology of Mamba can explicitly build the correlation among image patches or pixels. Recent studies have witnessed the effectiveness and efficiency of Mamba in various domains such as spatial and temporal. Therefore, we believe that introducing Mamba into its unexplored Fourier space to correlate different frequencies will improve image deraining.

In this paper, we propose a novel framework named FourierMamba, which performs image deraining using mamba in the Fourier domain. Following the "spatial interaction + channel evolution" rule that has also been validated on Mamba (Guo et al., 2024; Behrouz et al., 2024), we design the Mamba framework in the Fourier domain from both spatial and channel dimensions. Considering the unique arrangement of frequency orders in the Fourier domain, the core of FourierMamba lies in the scanning encoding of different frequencies, where the low-high frequency order formats unarranged in the spatial axis and arranged in the channel axis. Therefore, our proposed FourierMamba correlates Fourier space information in spatial and channel dimensions with distinct designs.

Specifically, **in the spatial dimension of the Fourier space**, low-high frequencies follow a concentric circular arrangement with lower frequencies near the center and higher frequencies around the periphery. If previous scanning method (Liu et al., 2024) is used directly, the orderliness between frequencies will be destroyed, as shown in Figure 1. We note that the zigzag coding in the JPEG compression field can place lower-frequency coefficients at the forefront of the array, while higher-frequency coefficients are positioned at the end. Hence, we introduce the zigzag coding to scan the frequency in the spatial dimension, rearranging the order from low to high frequency. Due to the symmetry of the frequency orders in the Fourier space, we do not directly

employ the zigzag coding in its originally used space; instead, we implement it in a circling-like manner that matches the symmetric frequency orders in Fourier space. In this way, this method orderly correlates the connections between frequencies, as shown in Figure 1. **In the channel dimension of the Fourier space**, the frequency order is arranged along the axis, following the order of low in the middle to high on both sides. Therefore, we can directly use Mamba for frequency correlation, thus improving channel information representation and enhancing global properties on the channels.

In summary, our contributions are as follows: (1) We propose a novel framework FourierMamba that combines Fourier priors and State Space Model for correlating different frequencies in the Fourier space to enhance image deraining. (2) To rearrange the order from low to high frequency in the spatial dimension Fourier space, we propose a scanning method based on zigzag coding to orderly correlate different frequencies. (3) Based on the channel-dimension Fourier transform, we utilize Mamba to scan on the channels and correlate different frequencies to improve channel information representation. Extensive experiments demonstrate that the proposed FourierMamba surpasses state-of-the-art methods both qualitatively and quantitatively.

## 2. Related Works

**Fourier transform.** Recently, the Fourier Transform has demonstrated its effectiveness in global modeling (Chi et al., 2019; 2020). This transformation converts signals into a domain characterized by global statistical properties, facilitating advancements across various fields (Huang et al., 2022; Lee et al., 2018; Li et al., 2023; Pratt et al., 2017; Xu et al., 2021; Yang & Soatto, 2020). Due to its efficacy in global modeling, the Fourier Transform has been introduced into low-level vision tasks (Fuoli et al., 2021; Mao et al., 2023). As an early attempt, (Fuoli et al., 2021) proposes

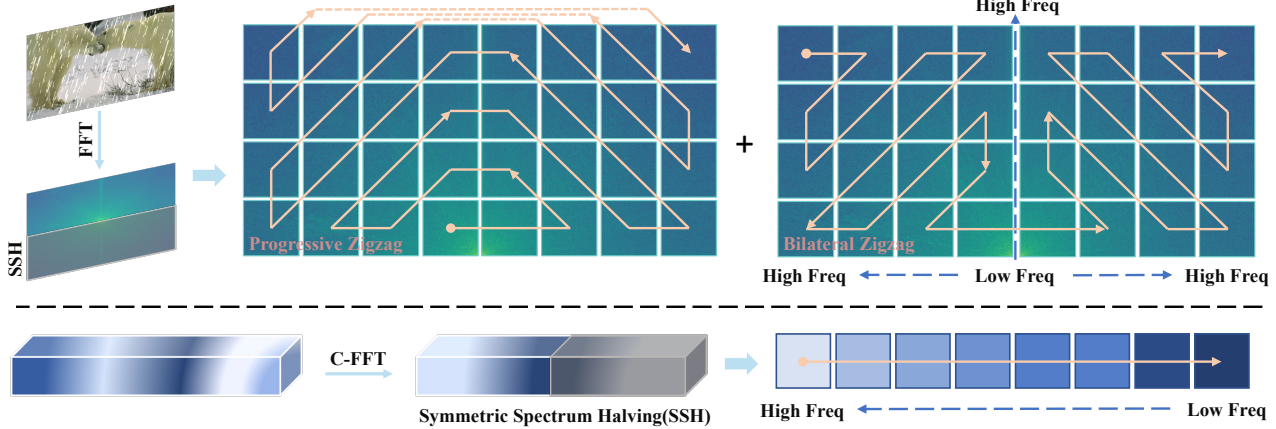


Figure 2. Our proposed Fourier space scanning method in the spatial dimension (top) and channel dimension (bottom). For simplicity, only one direction is shown for each scanning method, and in fact each method also performs a scan opposite to that shown.

a Fourier Transform-based loss to optimize global high-frequency information for efficient image super-resolution. DeepRFT (Mao et al., 2023) is proposed for image deblurring, employing a global receptive field to capture both low and high-frequency characteristics of various blurs, a concept similarly applied in image inpainting (Suvorov et al., 2022). FECNet (Huang et al., 2022) demonstrates that the amplitude of Fourier features decouples global luminance components, thereby proving effective for image enhancement. (Yu et al., 2022) observes a similar phenomenon in image dehazing, where the amplitude reflects global haze-related information. In contrast, we introduce a progressive scanning strategy in the Fourier domain, enhancing the global modeling capability while addressing the directional sensitivity issues of visual Mamba.

**State Space Models.** State Space Models (SSMs) have received a lot of attention recently due to their global modeling capabilities as well as linear complexity, with (Gu et al., 2022) initially introducing the base design of SSM models, and (Mehta et al., 2022) further enhancing their performance through gating units. More recently, the performance of Mamba (Gu & Dao, 2023), proposed based on selective scan mechanism and efficient hardware design, has seen significant enhancement. It stands as an efficient alternative to Transformers, finding applications in various domains including image classification (Zhu et al., 2024)(Liu et al., 2024), object detection(Chen et al., 2024), and remote sensing(Zhao et al., 2024). In the field of image restoration, (Guo et al., 2024) (Shi et al., 2024) initially introduced a general restoration framework based on the Mamba module but did not fully exploit the frequency domain information of images. (Sun et al., 2024) introduces a network combining Transformer and Mamba to capture long-range dependencies related to rain. (Yamashita & Ikebara, 2024) achieves effective deraining by parallelizing

frequency-domain processing branches with the Mamba branch. (Zhen et al., 2024) introduced a wavelet transform branch, yet the scanning in the wavelet domain fails to fully extract global frequency domain information. This paper proposes a novel Mamba restoration network based on Fourier transform, aiming to comprehensively exploit the frequency domain information of images. Please see the Appendix for more related works.

### 3. Methodology

#### 3.1. Preliminary

**Fourier transform.** Fourier transform is a widely used technique for analyzing the frequency content of an image. For images with multiple color channels, the Fourier transform is applied to each channel separately. Given an image  $X \in \mathbb{R}^{H \times W \times C}$ , the Fourier transform  $\mathcal{F}$  converts it to Fourier space as the complex component  $F(x)$ , which is expressed as:

$$F(x)(u, v) = \frac{1}{\sqrt{HW}} \sum_{h=0}^{H-1} \sum_{w=0}^{W-1} x(h, w) e^{-j2\pi(\frac{h}{H}u + \frac{w}{W}v)}, \quad (1)$$

where  $u$  and  $v$  indicate the coordinates of the Fourier space.  $\mathcal{F}^{-1}(x)$  defines the inverse Fourier transform accordingly. Both the Fourier transform and its inverse procedure can be efficiently implemented using FFT/IFFT algorithms (Frigo & Johnson, 1998). The amplitude component  $A(x)(u, v)$  and phase component  $P(x)(u, v)$  are expressed as:

$$\begin{aligned} A(x)(u, v) &= \sqrt{R^2(x)(u, v) + I^2(x)(u, v)}, \\ P(x)(u, v) &= \arctan \left[ \frac{I(x)(u, v)}{R(x)(u, v)} \right], \end{aligned} \quad (2)$$

where  $R(x)(u, v)$  and  $I(x)(u, v)$  represent the real and

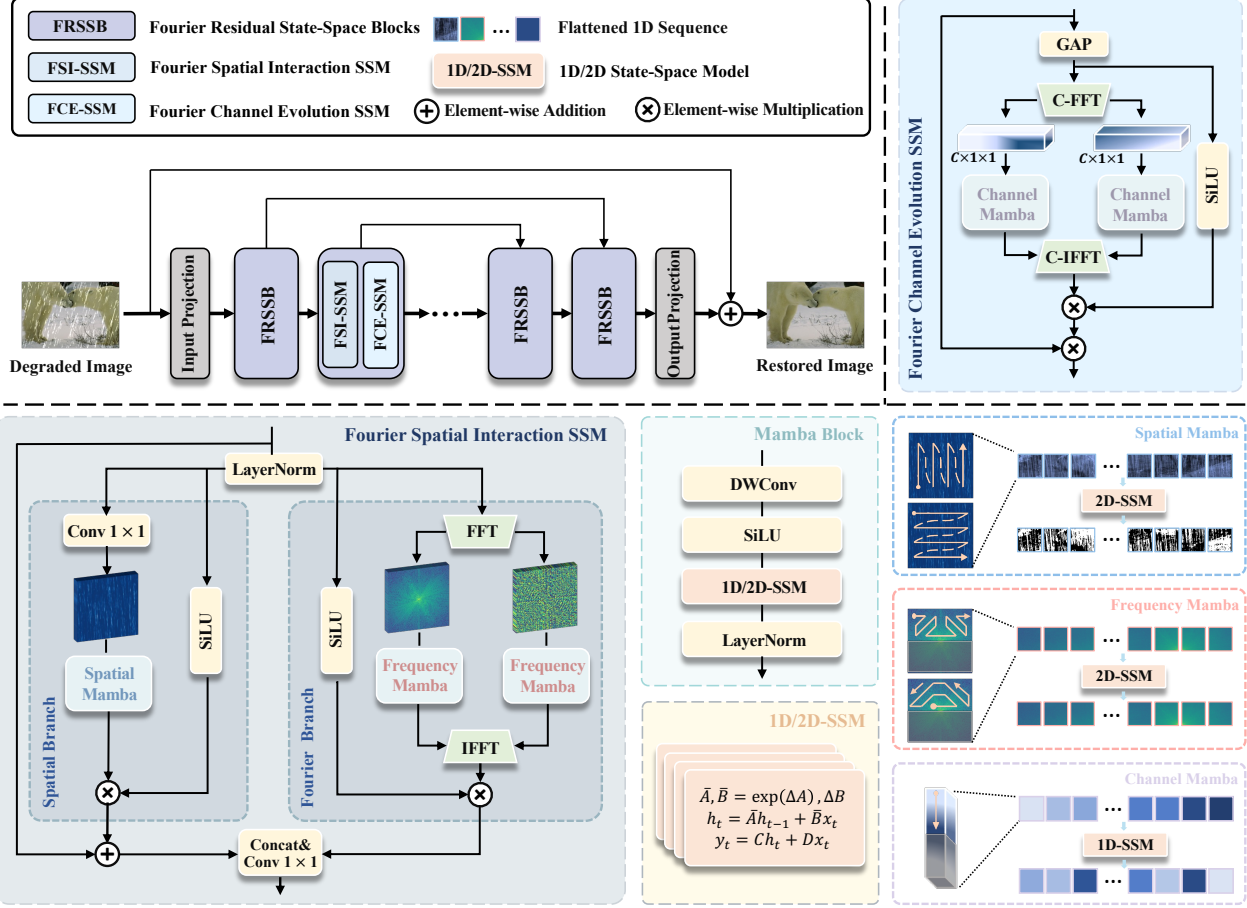


Figure 3. The overall architecture of the FourierMamba. Our FourierMamba consists of multiscale hierarchical design Fourier Residual State-Space Blocks(FRSSB). The core modules of FRSSB are Fourier Spatial Interaction SSM(FSI-SSM) and Fourier Channel Evolution SSM(FCE-SSM).

imaginary parts respectively. The Fourier transform and its inverse procedure are applied independently to each channel of the feature maps.

**Channel-dimension Fourier transform.** We introduce the channel-dimension Fourier transform (C-FFT) by individually applying the Fourier transform along the channel dimension for each spatial position. For each position ( $h \in \mathbb{R}^{H \times W \times C}$ ,  $w \in \mathbb{R}^{W \times 1}$ ) within  $X \in \mathbb{R}^{H \times W \times C}$ , denoted as  $x(h, w, 0 : C - 1)$  and abbreviated as  $y(0 : C - 1)$ , Fourier transform  $\mathcal{F}(\cdot)$  converts it to Fourier space as the complex component  $\mathcal{F}(y)$ , which is expressed as:

$$\mathcal{F}(y(0 : C - 1))(z) = \frac{1}{C} \sum_{c=0}^{C-1} y(c) e^{-j2\pi \frac{c}{C} z}, \quad (3)$$

Similarly, the amplitude component  $\mathcal{A}(y(0 : C - 1))(z)$  and phase component  $\mathcal{P}(y(0 : C - 1))(z)$  of  $\mathcal{F}(y(0 : C - 1))(z)$

are expressed as:

$$\begin{aligned} \mathcal{A}(y(0 : C - 1))(z) \\ = \sqrt{R^2(y(0 : C - 1))(z) + I^2(y(0 : C - 1))(z)}, \\ \mathcal{P}(y(0 : C - 1))(z) \\ = \arctan \left[ \frac{I(y(0 : C - 1))(z)}{R(y(0 : C - 1))(z)} \right]. \end{aligned}$$

These operations can also be applied for the global vector derived by the pooling operation. In this way,  $\mathcal{A}(z)$  and  $\mathcal{P}(z)$  signify the magnitude and directional changes in the magnitude of various channel frequencies, respectively. Both of these metrics encapsulate global statistics related to channel information.

**State Space Models.** State Space Models (SSMs) serve as the cornerstone for transforming one-dimensional inputs into outputs through latent states, utilizing a framework of linear ordinary differential equations. Mathematically, SSMs can be formulated as follows, representing linear

ordinary differential equations (ODEs):

$$\begin{aligned} h'(t) &= \mathbf{A}h(t) + \mathbf{B}x(t), \\ y(t) &= \mathbf{C}h(t) + \mathbf{D}x(t), \end{aligned} \quad (4)$$

where,  $h(t) \in \mathbb{R}^N$  denotes the hidden state vector, where  $N$  represents the size of the state. The parameters  $\mathbf{A} \in \mathbb{R}^{N \times N}$ ,  $\mathbf{B} \in \mathbb{R}^N$ , and  $\mathbf{C} \in \mathbb{R}^N$  are associated with the state size  $N$ , while  $\mathbf{D} \in \mathbb{R}^1$  represents the skip connection.

Discrete versions of these models, such as Mamba(Gu & Dao, 2023), include a discretization step via the zero-order hold (ZOH) method. This enables the models to adaptively scan and adjust to the input data using a selective scanning mechanism. This mechanism provides a global receptive field with linear complexity, which is advantageous for image restoration tasks.

### 3.2. Scanning in Fourier Space

Despite the unique characteristics of the selective scan mechanism (S6), it processes input data causally. Given the non-causal nature of visual data, directly applying this strategy to patches and flat images fails to estimate relations with unscanned patches, leading to a "directional sensitivity" issue constrained by the acceptance domain. Numerous methods have attempted to tackle this problem in the spatial domain (Liu et al., 2024; Guo et al., 2024). However, for image restoration, the Fourier space and its associated priors are crucial. Hence, we explore addressing the "directional sensitivity" issue within this domain. Specifically, we customize Fourier scanning strategies from both spatial and channel dimensions.

For the **spatial dimension**, each pixel point in the Fourier space contains global information, with its frequencies distributed in concentric circles. Scanning methods based on spatial arrangements (Liu et al., 2024) disrupt the high-low frequency relationships in the frequency domain, thus hindering the modeling of image degradation information.

Therefore, we aim to devise a scanning method in the Fourier space to progressively model the frequency characteristics of images. An intuitive approach is to calculate the Euclidean distance from each point in the spectrum to the center point. On the shifted Fourier spectrum, the smaller the distance to the center point, the lower the frequency. The flaw of this intuitive approach is that for images of different sizes, it requires recalculating the Euclidean distance from each point to the center point. The additional computational overhead introduced by this flaw makes this approach impractical in the field of image restoration.

In JPEG compression, zigzag coding is commonly used among the Discrete Cosine Transform (DCT) coefficients of JPEG, where it prioritizes the energy-concentrated low-frequency coefficients at the beginning of the array, and

places the less significant high-frequency coefficients towards the end, thereby facilitating more effective compression. Inspired by compression algorithms, we introduce a method that adopts the zigzag coding approach to scan the magnitude and phase spectra.

Additionally, due to the symmetry of the two-dimensional Fourier transform, scanning the entire spectrum would disrupt the symmetry in the Fourier space, potentially leading to the collapse of network optimization. Therefore, we scan half of the spectrum and then deduce the other half based on the central symmetry of the amplitude and the anti-central symmetry of the phase.

Specifically, we design two scanning strategies, as illustrated in the Figure 2. The first scanning method employs a dual zigzag pattern named **bilateral zigzag**, starting from the vertex of the highest frequency on one side of the spectrum, progressing in a zigzag pattern toward the center's low frequencies; similarly, it then zigzags to the opposite side's highest frequency. This scanning approach not only models the association between high and low frequencies but also takes into account the periodicity of the Fourier spectrum. Due to the periodic nature of the Fourier transform, the high-frequency ends on either side should, in fact, be contiguous. The second method builds upon the low-to-high frequency sequence established by zigzag scanning and conducts a scan from low to high frequencies, which is named **progressive zigzag**. This method is motivated by the tendency of neural networks to initially learn low-frequency information when extracting image characteristics. Following the previous method (Liu et al., 2024; Guo et al., 2024), we reverse the above two scanning methods as additional scanning directions.

For the **channel dimension** Fourier space, since it is a one-dimensional sequence arranged in order of low to high frequencies, we directly scan it one-dimensionally. Similarly, due to the symmetry of the Fourier transform, we scan only half and derive the other half. Through Fourier space scanning in both spatial and channel dimensions, we can correlate the connections between frequencies in an orderly manner, thereby making full use of frequency information to improve rain removal.

### 3.3. FourierMamba

#### 3.3.1. OVERALL FRAMEWORK

In Figure 3, we illustrate our proposed FourierMamba. Given a rainy image  $I \in \mathbb{R}^{H \times W \times 3}$ , FourierMamba first uses  $3 \times 3$  convolution layers to generate shallow features with dimensions of  $H \times W \times C$ , where  $H$  and  $W$  represent height and width, and  $C$  denotes the number of channels. Subsequently, we employ a multi-scale U-Net architecture to obtain deep features. This stage consists of a stack of

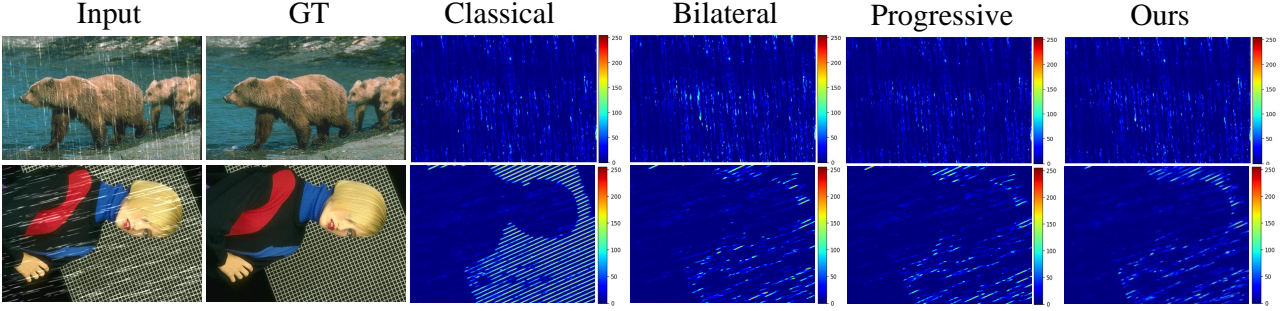


Figure 4. The error map between the GT and the restored images using various scanning methods in Fourier space. The two scanning methods we propose can achieve smaller errors than using classical scanning method (Liu et al., 2024). And the combination of the two scanning methods is better than either one.

Fourier Residual State-Space Groups, each containing several Fourier Residual State-Space Blocks (FRSSB). The FRSSB incorporates our two core designs: the Fourier Spatial Interaction SSM block and the Fourier Channel Evolution SSM block.

### 3.3.2. FOURIER SPATIAL INTERACTION SSM

The structure of the Fourier Spatial Interaction State Space Model (FSI-SSM) is shown in Figure 3. We first apply LayerNorm to transform the input features  $F_{in}$  into  $F_l$ . To facilitate the interaction between spatial and frequency information, FSI-SSM employs both a Fourier branch and a spatial branch to collaboratively process  $F_{in}$ .

**Fourier Branch:**  $F_l$  is transformed into the Fourier spectrum through the Fast Fourier Transform, subsequently decomposed into the amplitude spectrum  $\mathcal{A}(F_l)$  and phase spectrum  $\mathcal{P}(F_l)$ . The amplitude spectrum and phase spectrum are then processed separately using the progressive frequency scanning method illustrated in Figure 2 to obtain  $\mathcal{A}'(F_l)$  and  $\mathcal{P}'(F_l)$ .

$$\begin{aligned}\mathcal{A}'(F_l) &= \text{FourScan}(\mathcal{A}(F_l)), \\ \mathcal{P}'(F_l) &= \text{FourScan}(\mathcal{P}(F_l)),\end{aligned}\quad (5)$$

where FourScan is the sequence transformation using the Fourier space scan described in Sec. 3.2. Following a series of works (Liu et al., 2024; Guo et al., 2024; Zhen et al., 2024), the sequence transformation employs the following operation sequence:  $DWConv \rightarrow SiLU \rightarrow SSM \rightarrow LayerNorm$ . We then perform an inverse Fourier transform on the processed spectrum and multiply it with the output of SiLU.

$$F_f = (\mathcal{F}^{-1}(\mathcal{A}'(F_l), \mathcal{P}'(F_l))) \odot \text{SiLU}(F_l), \quad (6)$$

where  $F_f$  is the output of the fourier branch, and  $\odot$  is the Hadamard product.

**Spatial Branch** In the spatial domain, we feed the input features  $F_l$  into two parallel sub-branches. One sub-branch

activates the features using the SiLU function. The other sub-branch performs spatial Mamba on features after  $1 \times 1$  convolution. Specifically, spatial Mamba adopts the same operation sequence as the above frequency branch but the scanning in SSM uses the two-dimensional selective scanning module shown in Figure 3, which follows previous work (Liu et al., 2024; Guo et al., 2024). Finally, the outputs of the two sub-branches are multiplied element-wise to obtain the output  $F_s$ .

$$F_s = \text{SpaScan}(\text{Conv}(F_l)) \odot \text{SiLU}(F_l), \quad (7)$$

where Conv is  $1 \times 1$  convolution and SpaScan is the spatial Mamba mentioned above. Subsequently, we employ a residual connection to add the spatial output to  $F_{in}$ . The spatial branch captures global features in the spatial domain which complement the frequency correlations captured by the Fourier branch in the frequency domain, thereby benefiting the performance of image deraining. Hence, we concatenate the outputs of the spatial and frequency branches and use a  $1 \times 1$  convolution for the fusion of spatial and frequency information.

### 3.3.3. FOURIER CHANNEL EVOLUTION SSM

Previous work (Guo et al., 2024) claims that selecting key channels can avoid channel redundancy in SSM. Since each channel contains the information of all channels after the channel-dimension Fourier transform (C-FFT), we perform channel interaction in the Fourier domain to efficiently correlate different frequencies of channels. As depicted in Figure 3, our proposed Fourier Channel Evolution SSM (FCE-SSM) consists of three sequential parts: applying the Fourier transform along the channel dimension to obtain channel-wise Fourier domain features, scanning its amplitude and phase, then restoring to the spatial domain. Specifically, assuming the input features are denoted as  $F_r \in \mathbb{R}^{H_r \times W_r \times C_r}$ , we first perform global average pooling on it.

$$F_g = \frac{1}{H_r W_r} \sum_{h=0}^{H_r-1} \sum_{w=0}^{W_r-1} F_g(h, w), \quad (8)$$

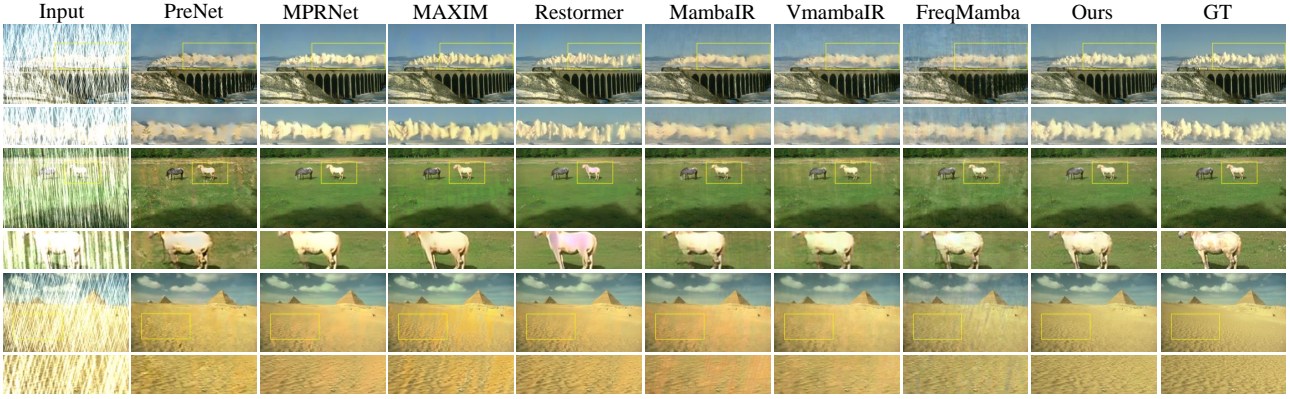


Figure 5. Qualitative comparison on Rain100H (Yang et al., 2017). Zoom in for better visualization.

where  $F_g \in \mathbb{R}^{1 \times 1 \times C_r}$  corresponds to the center point of the amplitude spectrum of  $F_r$  (see supplementary material), which effectively encapsulates the global information of the feature. Then, we use the channel-dimensional Fourier transform shown in Equ. 3 on  $F_g$  to obtain  $\mathcal{F}(F_g)(z)$ . Based on this, we use Equ. 4 for  $\mathcal{F}(F_g)(z)$  to obtain its amplitude component  $\mathcal{A}(F_g)(z)$  and phase component  $\mathcal{P}(F_g)(z)$ . Since the amplitude spectrum and phase spectrum have obvious information meaning, we choose to perform Mamba scanning on these two components.

$$\begin{aligned}\mathcal{A}(F_g)(z)' &= \text{ChaScan}(\mathcal{A}(F_g)(z)), \\ \mathcal{P}(F_g)(z)' &= \text{ChaScan}(\mathcal{P}(F_g)(z)),\end{aligned}\quad (9)$$

where ChaScan is a one-dimensional sequence transformation that uses the following sequence of operations:  $DWConv \rightarrow SiLU \rightarrow SSM \rightarrow LayerNorm$ . Its scanning method is shown in Figure 2. After the Mamba correlates different frequencies in the channel dimension, we perform an inverse Fourier transform on it and multiply the result with the channel features after SiLU activation.

$$F_a = (\mathcal{F}^{-1}(\mathcal{A}(F_g)(z)', \mathcal{P}(F_g)(z)')) \odot \text{SiLU}(F_g), \quad (10)$$

where  $F_a \in \mathbb{R}^{1 \times 1 \times C_r}$  is the channel feature after correlating different frequencies. Finally, we multiply it with the spatial feature in a form of attention to get the output  $F_c \in \mathbb{R}^{H_r \times W_r \times C_r}$ .

$$F_c = F_a \odot F_r. \quad (11)$$

### 3.3.4. OPTIMIZATION

We impose constraints in both the spatial and frequency domains. In the spatial domain, we utilize the L1 loss between the final output  $Y_{out}$  and the ground truth  $Y_{gt}$ . In the frequency domain, we apply the L1 loss based on the Fourier transform. The overall loss function is formulated as follows:

$$\mathcal{L}_{total} = \|Y_{out} - Y_{gt}\|_1 + \lambda \|\mathcal{F}(Y_{out}) - \mathcal{F}(Y_{gt})\|_1, \quad (12)$$

where  $\lambda$  is the balancing weight. In particular,  $\lambda$  is set to 0.02 empirically.

## 4. Experiment

### 4.1. Experimental Settings

**Datasets.** For training, we employ the widely used Rain13k dataset (Chen et al., 2021). It contains 13,712 image pairs in the training set, and we evaluate the results on Rain100H (Yang et al., 2017), Rain100L (Yang et al., 2017), Test2800 (Fu et al., 2017b), and Test1200 (Zhang & Patel, 2018).

**Evaluation Metrics.** Following previous work (Zamir et al., 2021; 2022), we adopt two commonly used quantitative metrics for evaluations: Peak Signal-to-Noise Ratio (PSNR) (Huynh-Thu & Ghanbari, 2008) and Structural Similarity Index (SSIM) (Wang et al., 2004).

**Implementation Details.** Our model is implemented within the PyTorch framework and executed on an NVIDIA A100 GPU. The number of blocks per layer has an impact on both the model’s parameter count and its deraining performance. After balancing the weights, we configure the blocks per layer as [2, 3, 3, 4, 3, 3, 2], which allows us to achieve commendable performance with a reasonable number of parameters. We adopt the progressive training strategy. Specifically, we set the total number of iterations to 80,000 and image sizes to [160, 256, 320, 384], with the corresponding batch sizes of [8, 4, 2, 1]. We utilize the Adam optimizer with default parameters. The initial learning rate is established at  $3 \times e^{-4}$ , followed by a gradual decay to  $1 \times e^{-6}$  using a cosine annealing schedule.

### 4.2. Comparison with State-of-the-art Methods

**Comparison on Benchmark Datasets.** We first verify the effectiveness of FourierMamba through training models on a mixture of synthetic datasets. We compare our method

Table 1. Quantitative comparison (PSNR/SSIM) for Image Deraining on five benchmark datasets. The highest and second-highest performances are marked in bold and underlined. ‘-’ indicates the result is not available.

Method	Venue	Rain100H (Yang et al., 2017) PNSR ↑ SSIM ↑	Rain100L (Yang et al., 2017) PNSR ↑ SSIM ↑	Test2800 (Fu et al., 2017b) PNSR ↑ SSIM ↑	Test1200 (Zhang & Patel, 2018) PNSR ↑ SSIM ↑	Param(M)	GFlops				
DerainNet (Fu et al., 2017b)	TIP'17	14.92	0.592	27.03	0.884	24.31	0.861	23.38	0.835	0.058	1.453
UMRL (Yasarla & Patel, 2019)	CVPR'19	26.01	0.832	29.18	0.923	29.97	0.905	30.55	0.910	0.98	-
RESCAN (Li et al., 2018)	ECCV'18	26.36	0.786	29.80	0.881	31.29	0.904	30.51	0.882	1.04	20.361
PreNet (Ren et al., 2019)	CVPR'19	26.77	0.858	32.44	0.950	31.75	0.916	31.36	0.911	0.17	73.021
MSPFN (Jiang et al., 2020)	CVPR'20	28.66	0.860	32.40	0.933	32.82	0.930	32.39	0.916	13.22	604.70
SPAIR (Purohit et al., 2021)	ICCV'21	30.95	0.892	36.93	0.969	33.34	0.936	33.04	0.922	-	-
MPRNet (Zamir et al., 2021)	CVPR'21	30.41	0.890	36.40	0.965	33.64	0.938	32.91	0.916	3.64	141.28
Restormer (Zamir et al., 2022)	CVPR'22	31.46	0.904	38.99	0.978	34.18	0.944	33.19	0.926	24.53	174.7
Fourmer (Zhou et al., 2023)	ICML'23	30.76	0.896	37.47	0.970	-	-	33.05	0.921	0.4	16.753
IR-SDE (Luo et al., 2023a)	ICML'23	31.65	0.904	38.30	0.980	30.42	0.891	-	-	135.3	119.1
MambaIR (Guo et al., 2024)	arxiv'24	30.62	0.893	38.78	0.977	33.58	0.927	32.56	0.923	31.51	80.64
VMambaIR (Shi et al., 2024)	arxiv'24	31.66	0.909	39.09	0.979	34.01	0.944	33.33	0.926	-	-
FreqMamba (Zhen et al., 2024)	arxiv'24	<u>31.74</u>	<u>0.912</u>	<u>39.18</u>	<u>0.981</u>	<b>34.25</b>	<b>0.951</b>	<u>33.36</u>	<u>0.931</u>	14.52	36.49
FourierMamba(Ours)	-	<b>31.79</b>	<b>0.913</b>	<b>39.73</b>	<b>0.986</b>	<b>34.23</b>	<b>0.949</b>	<b>34.76</b>	<b>0.938</b>	17.62	22.56



Figure 6. Qualitative comparison of real-world rainy images from Internet-Data (Wang et al., 2019).

with these deraining methods: DerainNet (Fu et al., 2017a), UMRL (Yasarla & Patel, 2019), RESCAN (Li et al., 2018), PreNet (Ren et al., 2019), MSPFN (Jiang et al., 2020), SPAIR (Purohit et al., 2021), MPRNet (Zamir et al., 2021), Restormer (Zamir et al., 2022), Fourmer (Zhou et al., 2023), IR-SDE (Luo et al., 2023b), MambaIR (Guo et al., 2024), VMambaIR (Shi et al., 2024) and FreqMamba (Zhen et al., 2024). Table 1 reports the performance evaluation on four datasets. It can be seen that our method achieves the best performance on most datasets, which emphasizes the effectiveness of FourierMamba in improving deraining performance.

To demonstrate the enhanced fidelity and detail levels exhibited by the images generated by our proposed FourierMamba, we compare the visual quality of challenging degraded images from the Rain100H dataset in Figure 5. Our method achieves excellent results when faced with complex or extremely severe rain streaks. Compared to previous methods, our FourierMamba achieves impeccable performance in both global and local restoration. For instance, by

zooming into the red boxed area in Figure 5, our method removes more rain streak residues while better restoring texture details.

#### Real-world Deraining Transferred from Synthetic Datasets.

To verify the generalization of the proposed method in real-world scenarios, we use the model trained on Rain13k to examine the real-world deraining capabilities. We evaluate the model trained on the synthetic dataset on the real-world dataset Internet-Data (Wang et al., 2019) without ground truth. As shown in Figure 6, FourierMamba is able to remove these complex rains and restore the clean background. In contrast, other deraining methods do not handle the effect of rain cleanly. More generalization results in real-world scenarios can be found in the Appendix.

#### Training On Real-world Rainy Datasets.

To further explore the potential of the proposed method, we use the real-world dataset SPADe (Wang et al., 2019) to train FourierMamba. In Table 2, our method is compared

**Table 2.** Quantitative comparison of training and testing on the real-world dataset SPA-Data.

Method	RESCAN	PReNet	SPDNet	DualGCN	Restormer	DRSformer	Ours
PSNR	38.11	40.16	43.20	44.18	47.98	48.54	<b>49.18</b>
SSIM	0.9707	0.9816	0.9871	0.9902	0.9921	0.9924	<b>0.9931</b>

**Table 3.** Ablation studies of key designs in the proposed method.

w/o FSI-SSM	w/o FCE-SSM	w/o SDF	w/o CDF	Ours
PSNR	39.05	39.08	38.25	38.72
SSIM	0.9835	0.9836	0.9810	0.9827

**Table 4.** Ablation of different scanning methods in Fourier space.

Classic(Liu et al., 2024)	Bilateral	Progressive	Ours
PSNR	38.82	39.31	39.28
SSIM	0.9817	0.9844	0.9843

with these methods RESCAN (Li et al., 2018), PReNet (Ren et al., 2019), SPDNet (Yi et al., 2021), DualGCN (Fu et al., 2021), Restormer (Zamir et al., 2022), and DRSformer (Chen et al., 2023a) with the same experimental settings. Surprisingly, we observe that FourierMamba acquires significant real-world rain removal capabilities. This shows that our method can effectively learn the precipitation model of real rain.

### 4.3. Ablation Studies

We perform ablations on the key designs and scanning methods of the framework on the Rain100L.

**Fourier Spatial Interaction SSM (FSI-SSM) and Fourier Channel Evolution SSM (FCE-SSM).** We replace the mamba scan in FSI-SSM and FCE-SSM with  $1 \times 1$  convolution, called w/o FSI-SSM and w/o FCE-SSM respectively. It can be seen from Table 3 that since  $1 \times 1$  convolution cannot model the dependence of different frequencies, its performance is worse than the mamba scan in the Fourier domain in both the spatial dimension and the channel dimension.

**Fourier prior.** We do not use Fourier transform in the spatial dimension and channel dimension respectively, but directly perform mamba scanning, which are called without spatial dimension Fourier (w/o SDF) and without channel dimension Fourier (w/o CDF) respectively. It can be seen from Table 3 that after losing the Fourier prior in the spatial dimension and channel dimension, the performance drops significantly. This proves the effectiveness of Fourier prior for removing rain from images. The Fourier prior also improves the visual effect; please refer to the Appendix.

**Scanning method in Fourier space.** We compare several scanning methods of the spatial dimension Fourier space, with the same amount of calculation. Table 4 illustrates that the performance of the two scanning methods we proposed is better than the classic two-dimensional scanning method (Liu et al., 2024). And thanks to complementarity, the combination of the two methods can also further improve performance. The visual comparison in Figure 4 supports this.

## 5. Conclusion

In this paper, we propose a novel image deraining framework, FourierMamba, which utilizes mamba to correlate frequencies in the Fourier space, thus fully exploiting frequency information. Specifically, we design the mamba framework by integrating the unique arrangement of frequency orderings within the Fourier domain across spatial and channel dimensions. In the spatial dimension, we devise two zigzag-based methods to scan frequencies, systematically correlating them. In the channel dimension, due to the ordered arrangement of frequencies along the axis, we directly apply mamba for frequency correlation. This work introduces a novel strategy to address the underutilization of frequency information in image deraining that affects performance. Extensive experiments on multiple benchmarks validate the effectiveness of the proposed method.

## Impact Statement

Due to uncontrollable weather conditions, image acquisition systems inevitably suffer interference from rain. Images captured during rainy conditions experience a significant decline in the quality of object details and contrast due to rain present in the air. Images tainted by rain can also severely impact the performance of outdoor computer vision systems, including autonomous driving and video surveillance. Therefore, image deraining itself holds significant research and application value. Our proposed FourierMamba combines the priors of Fourier space and the correlation modeling capability of Mamba, enabling the network to tackle more complex image deraining tasks. However, from a societal perspective, negative consequences might also follow. For instance, over-reliance on image deraining technology could introduce deviations from actual image textures, affecting effective judgment in autonomous driving and video surveillance. In these cases, it is necessary to combine expert knowledge to make rational decisions.

## Acknowledgement

This work is supported by the National Natural Science Foundation of China (NSFC) under Grants 62225207, 62436008, 62422609 and 62276243.

## References

- Ancuti, C. O., Ancuti, C., Sbert, M., and Timofte, R. Dense-haze: A benchmark for image dehazing with dense-haze and haze-free images. In *2019 IEEE international conference on image processing (ICIP)*, pp. 1014–1018. IEEE, 2019.
- Ancuti, C. O., Ancuti, C., and Timofte, R. Nh-haze: An image dehazing benchmark with non-homogeneous hazy and haze-free images. In *Proceedings of the IEEE/CVF conference on computer vision and pattern recognition workshops*, pp. 444–445, 2020.
- Behrouz, A., Santacatterina, M., and Zabih, R. Mambamixer: Efficient selective state space models with dual token and channel selection. *arXiv preprint arXiv:2403.19888*, 2024.
- Bozcan, I., Le Fevre, J., Pham, H. X., and Kayacan, E. Gridnet: Image-agnostic conditional anomaly detection for indoor surveillance. *IEEE Robotics and Automation Letters*, 6(2):1638–1645, 2021.
- Cai, B., Xu, X., Jia, K., Qing, C., and Tao, D. Dehazenet: An end-to-end system for single image haze removal. *IEEE transactions on image processing*, 25(11):5187–5198, 2016.
- Chen, L., Lu, X., Zhang, J., Chu, X., and Chen, C. Hinet: Half instance normalization network for image restoration. In *Proceedings of the IEEE/CVF Conference on Computer Vision and Pattern Recognition*, pp. 182–192, 2021.
- Chen, T., Tan, Z., Gong, T., Chu, Q., Wu, Y., Liu, B., Ye, J., and Yu, N. Mim-istd: Mamba-in-mamba for efficient infrared small target detection, 2024.
- Chen, X., Li, H., Li, M., and Pan, J. Learning a sparse transformer network for effective image deraining. In *Proceedings of the IEEE/CVF Conference on Computer Vision and Pattern Recognition*, pp. 5896–5905, 2023a.
- Chen, X., Pan, J., Dong, J., and Tang, J. Towards unified deep image deraining: A survey and a new benchmark. *arXiv preprint arXiv:2310.03535*, 2023b.
- Chi, L., Tian, G., Mu, Y., Xie, L., and Tian, Q. Fast non-local neural networks with spectral residual learning. In *Proceedings of the 27th ACM International Conference on Multimedia*, pp. 2142–2151, 2019.
- Chi, L., Jiang, B., and Mu, Y. Fast fourier convolution. *Advances in Neural Information Processing Systems*, 33: 4479–4488, 2020.
- Dong, H., Pan, J., Xiang, L., Hu, Z., Zhang, X., Wang, F., and Yang, M.-H. Multi-scale boosted dehazing network with dense feature fusion. In *Proceedings of the IEEE/CVF conference on computer vision and pattern recognition*, pp. 2157–2167, 2020.
- Frigo, M. and Johnson, S. G. Fftw: An adaptive software architecture for the fft. In *Proceedings of the 1998 IEEE International Conference on Acoustics, Speech and Signal Processing, ICASSP'98 (Cat. No. 98CH36181)*, volume 3, pp. 1381–1384. IEEE, 1998.
- Fu, X., Huang, J., Ding, X., Liao, Y., and Paisley, J. Clearing the skies: A deep network architecture for single-image rain removal. *IEEE Transactions on Image Processing*, 26(6):2944–2956, June 2017a. ISSN 1941-0042. doi: 10.1109/tip.2017.2691802. URL <http://dx.doi.org/10.1109/TIP.2017.2691802>.
- Fu, X., Huang, J., Zeng, D., Huang, Y., Ding, X., and Paisley, J. Removing rain from single images via a deep detail network. In *Proceedings of the IEEE conference on computer vision and pattern recognition*, pp. 3855–3863, 2017b.
- Fu, X., Qi, Q., Zha, Z.-J., Zhu, Y., and Ding, X. Rain streak removal via dual graph convolutional network. In *Proceedings of the AAAI Conference on Artificial Intelligence*, volume 35, pp. 1352–1360, 2021.
- Fu, X., Xiao, J., Zhu, Y., Liu, A., Wu, F., and Zha, Z.-J. Continual image deraining with hypergraph convolutional networks. *IEEE Transactions on Pattern Analysis and Machine Intelligence*, 45(8):9534–9551, 2023. doi: 10.1109/TPAMI.2023.3241756.
- Fu, Y.-H., Kang, L.-W., Lin, C.-W., and Hsu, C.-T. Single-frame-based rain removal via image decomposition. In *2011 IEEE International Conference on Acoustics, Speech and Signal Processing (ICASSP)*, pp. 1453–1456. IEEE, 2011.
- Fuoli, D., Van Gool, L., and Timofte, R. Fourier space losses for efficient perceptual image super-resolution. In *Proceedings of the IEEE/CVF International Conference on Computer Vision*, pp. 2360–2369, 2021.
- Gao, N., Jiang, X., Zhang, X., and Deng, Y. Efficient frequency-domain image deraining with contrastive regularization.
- Gu, A. and Dao, T. Mamba: Linear-time sequence modeling with selective state spaces, 2023.
- Gu, A., Goel, K., and Ré, C. Efficiently modeling long sequences with structured state spaces. In *The International Conference on Learning Representations (ICLR)*, 2022.

- Gu, S., Meng, D., Zuo, W., and Zhang, L. Joint convolutional analysis and synthesis sparse representation for single image layer separation. In *Proceedings of the IEEE international conference on computer vision*, pp. 1708–1716, 2017.
- Guo, C., Li, C., Guo, J., Loy, C. C., Hou, J., Kwong, S., and Cong, R. Zero-reference deep curve estimation for low-light image enhancement. In *Proceedings of the IEEE/CVF conference on computer vision and pattern recognition*, pp. 1780–1789, 2020.
- Guo, H., Li, J., Dai, T., Ouyang, Z., Ren, X., and Xia, S.-T. Mambair: A simple baseline for image restoration with state-space model. *arXiv preprint arXiv:2402.15648*, 2024.
- Guo, X., Fu, X., Zhou, M., Huang, Z., Peng, J., and Zha, Z.-J. Exploring fourier prior for single image rain removal. In *IJCAI*, pp. 935–941, 2022.
- He, K., Sun, J., and Tang, X. Single image haze removal using dark channel prior. *IEEE transactions on pattern analysis and machine intelligence*, 33(12):2341–2353, 2010.
- Hsu, W.-Y. and Chang, W.-C. Wavelet approximation-aware residual network for single image deraining. *IEEE transactions on pattern analysis and machine intelligence*, 2023.
- Huang, J., Liu, Y., Zhao, F., Yan, K., Zhang, J., Huang, Y., Zhou, M., and Xiong, Z. Deep fourier-based exposure correction network with spatial-frequency interaction. In *European Conference on Computer Vision*, pp. 163–180. Springer, 2022.
- Jiang, K., Wang, Z., Yi, P., Chen, C., Huang, B., Luo, Y., Ma, J., and Jiang, J. Multi-scale progressive fusion network for single image deraining. In *IEEE/CVF Conference on Computer Vision and Pattern Recognition (CVPR)*, June 2020.
- Jiang, L., Dai, B., Wu, W., and Loy, C. C. Focal frequency loss for image reconstruction and synthesis. In *Proceedings of the IEEE/CVF international conference on computer vision*, pp. 13919–13929, 2021.
- Lee, J.-H., Heo, M., Kim, K.-R., and Kim, C.-S. Single-image depth estimation based on fourier domain analysis. In *Proceedings of the IEEE conference on computer vision and pattern recognition*, pp. 330–339, 2018.
- Li, C., Guo, C.-L., Zhou, M., Liang, Z., Zhou, S., Feng, R., and Loy, C. C. Embedding fourier for ultra-high-definition low-light image enhancement. *arXiv preprint arXiv:2302.11831*, 2023.
- Li, X., Wu, J., Lin, Z., Liu, H., and Zha, H. Recurrent squeeze-and-excitation context aggregation net for single image deraining. In *European Conference on Computer Vision*, pp. 262–277. Springer, 2018.
- Li, Y., Tan, R. T., Guo, X., Lu, J., and Brown, M. S. Rain streak removal using layer priors. In *Proceedings of the IEEE conference on computer vision and pattern recognition*, pp. 2736–2744, 2016.
- Li, Y., Fang, C., Yang, J., Wang, Z., Lu, X., and Yang, M.-H. Universal style transfer via feature transforms. *Advances in neural information processing systems*, 30, 2017.
- Liu, L., Liu, B., Huang, H., and Bovik, A. C. No-reference image quality assessment based on spatial and spectral entropies. *Signal processing: Image communication*, 29(8):856–863, 2014.
- Liu, Y., Tian, Y., Zhao, Y., Yu, H., Xie, L., Wang, Y., Ye, Q., and Liu, Y. Vmamba: Visual state space model. *arXiv preprint arXiv:2401.10166*, 2024.
- Luo, Z., Gustafsson, F. K., Zhao, Z., Sjölund, J., and Schön, T. B. Image restoration with mean-reverting stochastic differential equations. *International Conference on Machine Learning*, 2023a.
- Luo, Z., Gustafsson, F. K., Zhao, Z., Sjölund, J., and Schön, T. B. Refusion: Enabling large-size realistic image restoration with latent-space diffusion models. In *Proceedings of the IEEE/CVF Conference on Computer Vision and Pattern Recognition Workshops*, pp. 1680–1691, 2023b.
- Mao, X., Liu, Y., Liu, F., Li, Q., Shen, W., and Wang, Y. Intriguing findings of frequency selection for image deblurring. In *Proceedings of the AAAI Conference on Artificial Intelligence*, volume 37, pp. 1905–1913, 2023.
- Mehta, H., Gupta, A., Cutkosky, A., and Neyshabur, B. Long range language modeling via gated state spaces. *arXiv preprint arXiv:2206.13947*, 2022.
- Mittal, A., Moorthy, A. K., and Bovik, A. C. No-reference image quality assessment in the spatial domain. *IEEE Transactions on image processing*, 21(12):4695–4708, 2012a.
- Mittal, A., Soundararajan, R., and Bovik, A. C. Making a “completely blind” image quality analyzer. *IEEE Signal processing letters*, 20(3):209–212, 2012b.
- Pratt, H., Williams, B., Coenen, F., and Zheng, Y. Fcnn: Fourier convolutional neural networks. In *Machine Learning and Knowledge Discovery in Databases: European Conference, ECML PKDD 2017, Skopje, Macedonia, September 18–22, 2017, Proceedings, Part I* 17, pp. 786–798. Springer, 2017.

- Purohit, K., Suin, M., Rajagopalan, A., and Boddeti, V. N. Spatially-adaptive image restoration using distortion-guided networks. In *Proceedings of the IEEE/CVF International Conference on Computer Vision*, pp. 2309–2319, 2021.
- Quan, R., Yu, X., Liang, Y., and Yang, Y. Removing raindrops and rain streaks in one go. In *Proceedings of the IEEE/CVF conference on computer vision and pattern recognition*, pp. 9147–9156, 2021.
- Ran, W., Yang, Y., and Lu, H. Single image rain removal boosting via directional gradient. In *2020 IEEE International Conference on Multimedia and Expo (ICME)*, pp. 1–6. IEEE, 2020.
- Ran, W., Ma, P., He, Z., Ren, H., and Lu, H. Harnessing joint rain-/detail-aware representations to eliminate intricate rains. In *International Conference on Learning Representations*, 2024.
- Ren, D., Zuo, W., Hu, Q., Zhu, P., and Meng, D. Progressive image deraining networks: A better and simpler baseline. In *IEEE Conference on Computer Vision and Pattern Recognition*, 2019.
- Shi, Y., Xia, B., Jin, X., Wang, X., Zhao, T., Xia, X., Xiao, X., and Yang, W. Vmambair: Visual state space model for image restoration. *arXiv preprint arXiv:2403.11423*, 2024.
- Sun, S., Ren, W., Zhou, J., Gan, J., Wang, R., and Cao, X. A hybrid transformer-mamba network for single image deraining. *arXiv preprint arXiv:2409.00410*, 2024.
- Suvorov, R., Logacheva, E., Mashikhin, A., Remizova, A., Ashukha, A., Silvestrov, A., Kong, N., Goka, H., Park, K., and Lempitsky, V. Resolution-robust large mask inpainting with fourier convolutions. In *Proceedings of the IEEE/CVF winter conference on applications of computer vision*, pp. 2149–2159, 2022.
- Valanarasu, J. M. J., Yasarla, R., and Patel, V. M. Tran-sweathe: Transformer-based restoration of images degraded by adverse weather conditions. In *Proceedings of the IEEE/CVF Conference on Computer Vision and Pattern Recognition*, pp. 2353–2363, 2022.
- Wang, C., Pan, J., and Wu, X.-M. Online-updated high-order collaborative networks for single image deraining. In *Proceedings of the AAAI Conference on Artificial Intelligence*, volume 36, pp. 2406–2413, 2022a.
- Wang, H., Xie, Q., Zhao, Q., and Meng, D. A model-driven deep neural network for single image rain removal. In *Proceedings of the IEEE/CVF conference on computer vision and pattern recognition*, pp. 3103–3112, 2020.
- Wang, T., Yang, X., Xu, K., Chen, S., Zhang, Q., and Lau, R. W. Spatial attentive single-image deraining with a high quality real rain dataset. In *Proceedings of the IEEE/CVF conference on computer vision and pattern recognition*, pp. 12270–12279, 2019.
- Wang, Z., Cun, X., Bao, J., Zhou, W., Liu, J., and Li, H. Uformer: A general u-shaped transformer for image restoration. In *Proceedings of the IEEE/CVF conference on computer vision and pattern recognition*, pp. 17683–17693, 2022b.
- Wei, C., Wang, W., Yang, W., and Liu, J. Deep retinex decomposition for low-light enhancement. *arXiv preprint arXiv:1808.04560*, 2018.
- Wu, H., Qu, Y., Lin, S., Zhou, J., Qiao, R., Zhang, Z., Xie, Y., and Ma, L. Contrastive learning for compact single image dehazing. In *Proceedings of the IEEE/CVF conference on computer vision and pattern recognition*, pp. 10551–10560, 2021.
- Wu, W., Weng, J., Zhang, P., Wang, X., Yang, W., and Jiang, J. Uretinex-net: Retinex-based deep unfolding network for low-light image enhancement. In *Proceedings of the IEEE/CVF conference on computer vision and pattern recognition*, pp. 5901–5910, 2022.
- Xiao, J., Fu, X., Liu, A., Wu, F., and Zha, Z.-J. Image de-raining transformer. *IEEE Transactions on Pattern Analysis and Machine Intelligence*, 2022.
- Xu, Q., Zhang, R., Zhang, Y., Wang, Y., and Tian, Q. A fourier-based framework for domain generalization. In *Proceedings of the IEEE/CVF conference on computer vision and pattern recognition*, pp. 14383–14392, 2021.
- Xu, X., Wang, R., Fu, C.-W., and Jia, J. Snr-aware low-light image enhancement. In *Proceedings of the IEEE/CVF conference on computer vision and pattern recognition*, pp. 17714–17724, 2022.
- Yamashita, S. and Ikebara, M. Image deraining with frequency-enhanced state space model. *arXiv preprint arXiv:2405.16470*, 2024.
- Yang, W., Tan, R. T., Feng, J., Liu, J., Guo, Z., and Yan, S. Deep joint rain detection and removal from a single image. In *Proceedings of the IEEE conference on computer vision and pattern recognition*, pp. 1357–1366, 2017.
- Yang, Y. and Soatto, S. Fda: Fourier domain adaptation for semantic segmentation. In *Proceedings of the IEEE/CVF conference on computer vision and pattern recognition*, pp. 4085–4095, 2020.
- Yasarla, R. and Patel, V. M. Uncertainty guided multi-scale residual learning-using a cycle spinning cnn for single

- image de-raining. In *The IEEE Conference on Computer Vision and Pattern Recognition (CVPR)*, June 2019.
- Yi, Q., Li, J., Dai, Q., Fang, F., Zhang, G., and Zeng, T. Structure-preserving deraining with residue channel prior guidance. In *Proceedings of the IEEE/CVF international conference on computer vision*, pp. 4238–4247, 2021.
- Yu, H., Zheng, N., Zhou, M., Huang, J., Xiao, Z., and Zhao, F. Frequency and spatial dual guidance for image dehazing. In *European Conference on Computer Vision*, pp. 181–198. Springer, 2022.
- Zamir, S. W., Arora, A., Khan, S., Hayat, M., Khan, F. S., Yang, M.-H., and Shao, L. Multi-stage progressive image restoration. In *CVPR*, 2021.
- Zamir, S. W., Arora, A., Khan, S., Hayat, M., Khan, F. S., and Yang, M.-H. Restormer: Efficient transformer for high-resolution image restoration. In *CVPR*, 2022.
- Zhang, H. and Patel, V. M. Density-aware single image de-raining using a multi-stream dense network. In *Proceedings of the IEEE conference on computer vision and pattern recognition*, pp. 695–704, 2018.
- Zhang, Y., Zhang, J., and Guo, X. Kindling the darkness: A practical low-light image enhancer. In *Proceedings of the 27th ACM international conference on multimedia*, pp. 1632–1640, 2019.
- Zhang, Y., Guo, X., Ma, J., Liu, W., and Zhang, J. Beyond brightening low-light images. *International Journal of Computer Vision*, 129:1013–1037, 2021.
- Zhao, S., Chen, H., Zhang, X., Xiao, P., Bai, L., and Ouyang, W. Rs-mamba for large remote sensing image dense prediction, 2024.
- Zhen, Z., Hu, Y., and Feng, Z. Freqmamba: Viewing mamba from a frequency perspective for image deraining, 2024.
- Zhou, M., Huang, J., Guo, C.-L., and Li, C. Fourmer: An efficient global modeling paradigm for image restoration. In *International Conference on Machine Learning*, pp. 42589–42601. PMLR, 2023.
- Zhu, L., Liao, B., Zhang, Q., Wang, X., Liu, W., and Wang, X. Vision mamba: Efficient visual representation learning with bidirectional state space model, 2024.

## A. Appendix

### A.1. Limitation

In this work, we introduce FourierMamba and extensively validate its efficacy for image deraining through experiments. Our experiments primarily leverage the widely used U-shaped architecture. We plan to further validate the effectiveness of combining Fourier priors with Mamba on more architectures, such as isotropic and multi-stage architecture.

Furthermore, given the proven priors of Fourier transform for capturing rain streaks, we choose to first validate FourierMamba on image deraining. Our work could also offer novel insights for other low-level vision fields, though it may necessitate integrating priors tailored to the distinct differences between various low-level tasks. Given the universal need across various low-level tasks for Fourier priors and the importance of correlating frequencies, the performing improvements can be positively anticipated. We will explore applications in other low-level tasks in our future work.

### A.2. More related works

**Image deraining.** Traditional image deraining methods focus on separating rain components by utilizing meticulously designed priors, such as Gaussian Mixture Models (Li et al., 2016), Sparse Representation Learning (Gu et al., 2017; Fu et al., 2011), and Directional Gradient Priors (Ran et al., 2020). Although these methods are insightful, they often struggle to cope with complex precipitation patterns and the diverse real-world scenarios. The advent of deep learning has heralded a new era for image deraining. (Fu et al., 2017b) introduces pioneering deep residual networks for image deraining. The initiation of CNNs marked a significant advancement, facilitating more nuanced and adaptive processing of rain streaks across a vast array of images (Yang et al., 2017; Zhang & Patel, 2018). With the evolution of transformers, the development of architectures that incorporate attention mechanisms (Valanarasu et al., 2022; Wang et al., 2022b) has further refined the capacity to recognize and eliminate rain components, addressing previous shortcomings in model generalization and detail preservation. COIC (Ran et al., 2024) presents a Context-based Instance-level Modulation mechanism integrated with rain-/detail-aware contrastive learning to enhance CNN and Transformer models for improved image deraining on mixed datasets. (Hsu & Chang, 2023) proposes a wavelet approximation-aware residual network, which efficiently removes rain from low-frequency structures and high-frequency details at each level separately. In this work, we propose a novel baseline with a block based on Fourier and Mamba to enhance deraining performance.

### A.3. Inference time of the model

In this section, we compare the inference time of the proposed method with several state-of-the-art methods. The comparison results of the model inference time using  $512 \times 512$  images on NVIDIA RTX 4090 GPU are shown in Table 5. It can be seen that the inference time of our model is comparable to that of other methods.

Table 5. Runtime comparison between our method and other approaches.

Method	Mambair	Vmambair	FreqMamba	Restormer	Ours
Runtime (s)	0.534s	0.423s	1.837s	0.253s	0.523s

### A.4. Results on test100

In this section, we add some performance comparisons with other methods on Test100 as shown in Table 6. All methods are trained on rain13k and then tested on Test100. It can be seen that our method still achieves excellent deraining performance.

Table 6. Performance comparison on Test100. PSNR ( $\uparrow$ ) and SSIM ( $\uparrow$ ) are reported.

Metric	PReNet	MPRNet	Restormer	Mambair	Vmambair	FreqMamba	Ours
PSNR	24.81	30.27	32.00	31.82	31.84	31.89	32.07
SSIM	0.851	0.897	0.923	0.922	0.918	0.921	0.925

### A.5. Ablation studies and computational overhead

To further demonstrate the effectiveness of Mamba, we present the impact of computational overhead in the first ablation study. For the ablation of FSI-SSM, we compress our model by reducing the number of channels and blocks, achieving a

computational cost similar to that of the "w/o FSI-SSM" variant. The comparison is shown in Table 7. As observed, the model with FSI-SSM still achieves better performance. For the ablation of FCE-SSM, the computational overhead of the variant without FCE-SSM (w/o FCE-SSM) in Table 3 is similar to that of the model with FCE-SSM. The "w/o FCE-SSM" variant stacks several  $1 \times 1$  convolutions with residual connections to match the parameter count of Mamba. The specific computational overhead and performance are shown in Table 8. It is evident that, with a similar parameter count, our method outperforms the "w/o FCE-SSM" variant.

Table 7. The computational overhead of the ablation study on FSI-SSM.

Method	PSNR	SSIM	Flops(G)	Params(M)
w/o FSI-SSM	39.05	0.9835	14.42	10.82
<b>Ours</b>	39.37	0.9845	14.64	10.12

Table 8. The computational overhead of the ablation study on FCE-SSM.

Method	PSNR	SSIM	Flops(G)	Params(M)
w/o FCE-SSM	39.08	0.9836	21.08	17.81
<b>Ours</b>	39.73	0.9856	22.56	17.62

#### A.6. Reasons for using channel-dimensional Fourier

To address the limitation of Fourier transform not accounting for channel evolution, we introduce channel-dimension Fourier transform. A pivotal motivation is due to different channels often displaying varying properties of degradation information, which also determine the global information of the image when conjunct different channels. A comparable deduction can be drawn from style transfer research, where the Gram matrix signifies global style information (Li et al., 2017). This inspires us to employ Fourier transform on the channel dimension to enrich the representation of global information.

#### A.7. The Relationship between Global Average Pooling and Fourier Transform

We believe that the global average pooling equals  $\mathcal{A}(0, 0)$  in the amplitude. In the Appendix, we further verify this. Typically, the Spatail Fourier transform is expressed as:

$$\mathcal{F}(x)(u, v) = \frac{1}{\sqrt{HW}} \sum_{h=0}^{H-1} \sum_{w=0}^{W-1} x(h, w) e^{-j2\pi(\frac{h}{H}u + \frac{w}{W}v)}. \quad (13)$$

The center point of the amplitude spectrum means that  $u$  and  $v$  are 0. The formula is as follows:

$$\mathcal{F}(x)(0, 0) = \frac{1}{\sqrt{HW}} \sum_{h=0}^{H-1} \sum_{w=0}^{W-1} x(h, w). \quad (14)$$

It can be seen that the above formula is essentially to find the average value of the entire feature map. Therefore, global average pooling (GAP) is equivalent to taking the center point of the amplitude spectrum.

#### A.8. Performance on other low-level vision tasks

To further demonstrate the effectiveness of our approach, we investigate the performance of our model on other low-level vision tasks. Following FreqMamba (Zhen et al., 2024), we evaluate our method on low-light enhancement and image dehazing. We use the LOL-V1 (Wei et al., 2018) and LOL-V2-synthetic (Wei et al., 2018) datasets to evaluate the performance of our method on low-light enhancement, and the Dense-Haze (Ancuti et al., 2019) and NH-HAZE (Ancuti et al., 2020) datasets are used to evaluate the performance of our method on real-world image dehazing. The results for low-light enhancement are shown in the Table 9. The comparison results for image dehazing are presented in the Table 10. It can be seen that our method also demonstrates significant potential for other image restoration tasks.

#### A.9. Differences between the proposed method and FreqMamba

Our method focuses on customized design based on the characteristics of Fourier space, combining Fourier priors with state space models and exploring the potential of introducing Mamba directly in the Fourier domain. In contrast, FreqMamba

Table 9. Comparison of methods on LOL-V1 and LOL-V2-Syn datasets.

Method	LOL-V1		LOL-V2-Syn	
	PSNR ↑	SSIM ↑	PSNR ↑	SSIM ↑
RetinexNet (Wei et al., 2018)	18.38	0.7756	19.92	0.8847
KinD (Zhang et al., 2019)	20.38	0.8248	22.62	0.9041
ZeroDCE (Guo et al., 2020)	16.8	0.5573	17.53	0.6072
KinD++ (Zhang et al., 2021)	21.3	0.8226	21.17	0.8814
URetinex-Net (Wu et al., 2022)	21.33	0.8348	22.89	0.895
FECNet (Huang et al., 2022)	22.24	0.8372	22.57	0.8938
SNR-Aware (Xu et al., 2022)	23.38	0.8441	24.12	0.9222
FreqMamba (Zhen et al., 2024)	23.57	0.8453	24.46	0.9355
Ours	<b>23.78</b>	<b>0.8467</b>	<b>24.75</b>	<b>0.9452</b>

Table 10. Comparison of methods on Dense-Haze and NH-HAZE datasets.

Method	Dense-Haze		NH-HAZE	
	PSNR ↑	SSIM ↑	PSNR ↑	SSIM ↑
DCP (He et al., 2010)	10.06	0.3856	10.57	0.5196
DehazeNet (Cai et al., 2016)	13.84	0.4252	16.62	0.5238
GridNet (Bozcan et al., 2021)	13.31	0.3681	13.80	0.5370
MSBDN (Dong et al., 2020)	15.37	0.4858	19.23	0.7056
AECR-Net (Wu et al., 2021)	15.80	0.4660	19.88	0.7173
FreqMamba (Zhen et al., 2024)	17.35	0.5827	19.93	0.7372
Ours	<b>18.91</b>	<b>0.6763</b>	<b>20.03</b>	<b>0.7508</b>

operates in the Fourier space using only  $1 \times 1$  convolutions, which fails to fully utilize the rich frequency information inherent to the Fourier domain. Specifically, FreqMamba applies Mamba scanning in a wavelet-transformed domain. However, the wavelet-transformed domain lacks the notable advantages of the Fourier domain, such as the Fourier transform's ability to decouple degradations and its global representation properties. Additionally, after wavelet decomposition, FreqMamba divides the image into multiple patches and performs spatial scanning within each patch. This design limits FreqMamba's ability to effectively model frequency correlations.

In contrast, our method performs Mamba scanning directly in the Fourier domain, fully leveraging the global characteristics of the Fourier transform. This allows our approach to better capture rain streaks, which often exhibit high apparent repetitiveness. Consequently, from a visual perspective, our method demonstrates significantly better performance in removing rain streaks. As shown in Figure 7, we show the feature maps and restoration results of FreqMamba and our method. It can be seen that our method can better capture the rain lines and thus remove the rain lines more cleanly.

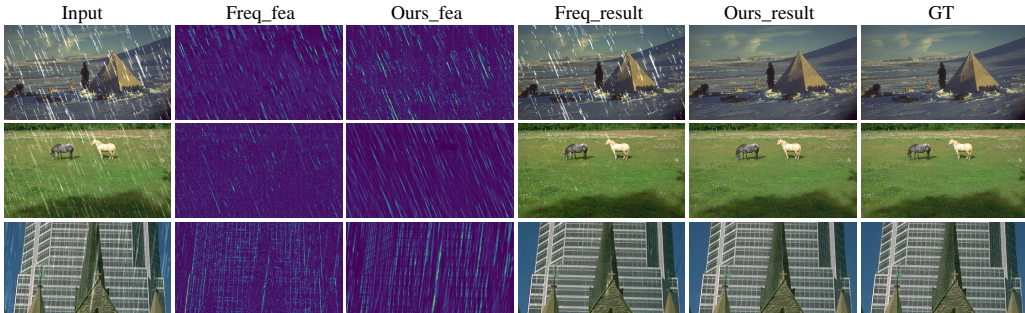


Figure 7. Feature maps and restoration results of FreqMamba and our method.

#### A.10. Comparison with other methods such as DRSformer and FADformer

In this section, we compare our method with RCDNet (Wang et al., 2020), MPRNet (Zamir et al., 2021), SPDNet (Yi et al., 2021), DualGCN (Fu et al., 2021), HCN (Fu et al., 2023), Uformer (Wang et al., 2022b), IDT (Xiao et al., 2022), Restormer (Zamir et al., 2022), DRSformer (Chen et al., 2023a) and FADformer (Gao et al.), as shown in Table 11. To ensure fairness, we adopt the same experimental setup as the other methods, performing independent training and testing on each dataset, including Rain200L/H (Yang et al., 2017), DID-Data (Zhang & Patel, 2018), DDN-Data (Fu et al., 2017b), and SPA (Wang et al., 2019). The results demonstrate that our method achieves superior performance on the majority of the datasets.

Table 11. Performance comparison of methods across various datasets.

Method	Rain200L		Rain200H		DID-Data		DDN-Data		SPA-Data		Average	
	PSNR ↑	SSIM ↑										
RCDNet	39.17	0.9885	30.24	0.9048	34.08	0.9532	33.04	0.9472	43.36	0.9831	35.97	0.9554
MPRNet	39.47	0.9825	30.67	0.911	33.99	0.959	33.1	0.9347	43.64	0.9844	36.17	0.9543
SPDNet	40.5	0.9875	31.28	0.9207	34.57	0.956	33.15	0.9457	43.2	0.9871	36.54	0.9594
DualGCN	40.73	0.9886	31.15	0.9125	34.37	0.962	33.01	0.9489	44.18	0.9902	36.68	0.9604
HCN	41.31	0.9892	31.34	0.9248	34.7	0.9613	33.42	0.9512	45.03	0.9907	37.16	0.9634
Uformer	40.2	0.986	30.8	0.9105	35.02	0.9621	33.95	0.9545	46.13	0.9913	37.22	0.9609
IDT	40.74	0.9884	32.1	0.9344	34.89	0.9623	33.84	0.9549	47.35	0.993	37.78	0.9666
Restormer	40.99	0.989	32.0	0.9329	35.29	0.9641	34.20	0.9571	47.98	0.9921	38.09	0.9670
DRSformer	41.23	0.9894	32.17	0.9326	35.35	0.9646	34.35	0.9588	48.54	0.9924	38.32	0.9676
FADformer	41.80	0.9906	32.48	0.9359	35.48	0.9657	34.42	<b>0.9602</b>	<b>49.21</b>	<b>0.9934</b>	38.67	0.9691
Ours	<b>42.27</b>	<b>0.9908</b>	<b>32.71</b>	<b>0.9395</b>	<b>35.49</b>	<b>0.9659</b>	<b>35.58</b>	0.9599	49.18	0.9931	<b>39.05</b>	<b>0.9698</b>

### A.11. Difference between mamba and convolution in processing Fourier frequencies

First, Mamba utilizes sequence modeling to integrate information across all frequency bands, effectively leveraging the complementary relationships between different bands. In contrast, convolution, as a local operation, struggles to holistically model global features across all frequency bands when processing frequency information in the Fourier domain. This limitation significantly constrains its capacity in the Fourier space. Second, Mamba’s sequence modeling is orderly, which can help the network establish an orderly dependency relationship between different frequencies. This characteristic is critical for modeling image degradation information. Conversely, convolution is insufficient in capturing the dependencies between high and low frequencies in the Fourier domain, thereby weakening its ability to accurately represent degradation features. In summary, based on these two advantages, Mamba achieves better coordination of high-frequency and low-frequency information in the Fourier domain during the image restoration process.

We process the Fourier frequencies using both Mamba and convolution separately, and then visualize their features, as shown in Figure 8. It can be seen our method (i.e., Mamba) not only captures rain streaks effectively but also extracts structural information from the background with high accuracy.

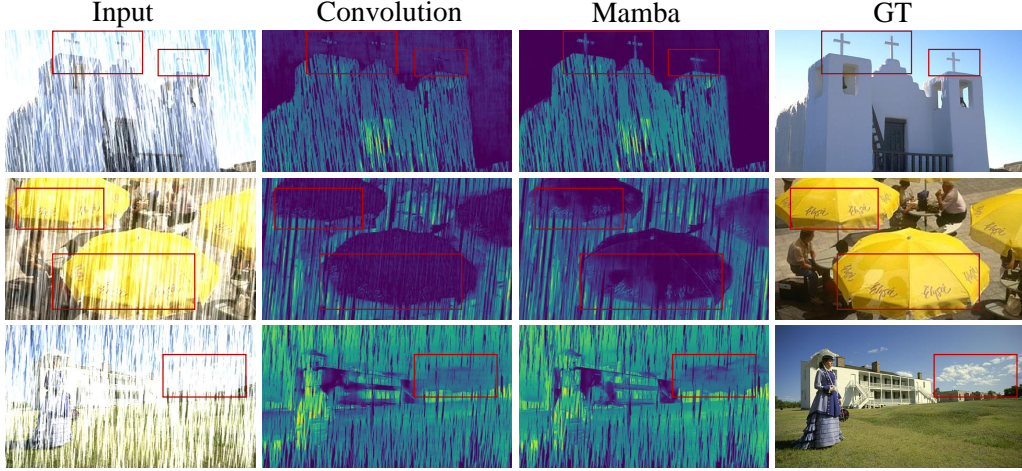


Figure 8. Feature visualization comparison of frequency-domain convolution and mamba on Rain100H.

### A.12. More visual deaining comparison on synthetic datasets

In this section, we provide more visual deraining comparisons on synthetic datasets to further demonstrate the effectiveness of our method. Specifically, we perform visual comparisons on several datasets in Table 1. Figure 9 shows more visualization results on Rain100H. As with the results in the main text, it shows that our method can better remove rain effects and prevent artifacts, which is attributed to the progressive frequency correlation. Figures 10, 11, and 12 show the visualization results

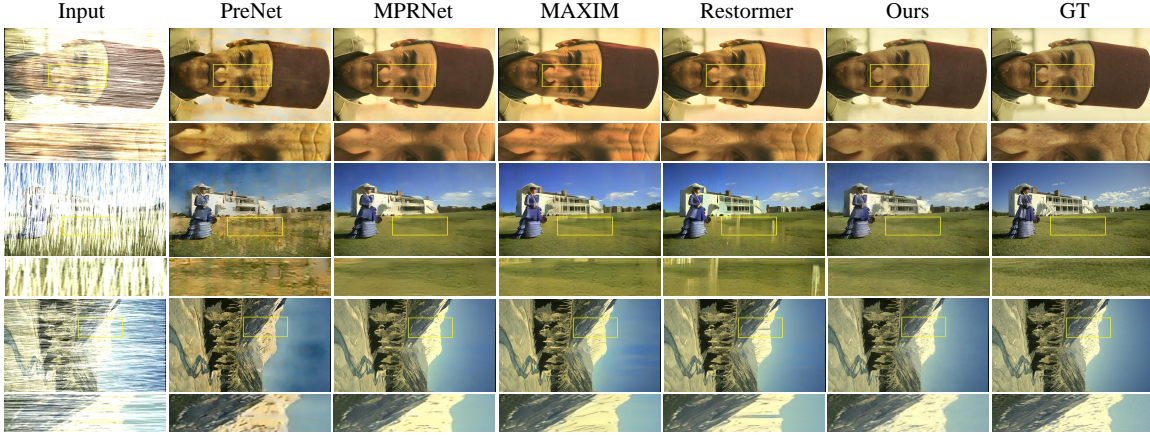


Figure 9. More qualitative comparison on Rain100H (Yang et al., 2017).

Table 12. Quantitative comparison of testing on the real-world dataset SPA-Data.

Method	PReNet	RESCAN	HiNet	MSPFN	Restormer	MPRNet	Ours
PSNR	31.33	31.56	33.89	34.03	34.18	34.54	<b>35.27</b>
SSIM	0.9501	0.9423	0.9500	0.9471	0.9493	0.9548	<b>0.9575</b>

on the simulation datasets Rain100L, Test2800, and Test1200, respectively.

### A.13. More real-world detraining results by using synthetic data

In this section, we provide more real-world rain removal cases to verify the generalization ability of the model trained on the synthetic dataset (rain13k). The quantitative comparisons directly tested on SPA-Data are shown in Table 12. The visualization results are shown in Figure 13. Our method is superior to other methods in rain removal and detail recovery. To further demonstrate its generalization ability in the real world, we also tested it on a real-world dataset RE-RAIN —(Chen et al., 2023b), as shown in Figure 14. FourierMamba can obtain the most visually pleasing results. In addition, we also tested our method directly on RainDS-Real (Quan et al., 2021), and the quantitative results are shown in the table 13. Figure 15 shows the visualization results on RainDS-Real. It can be seen that our method can effectively remove real rain.

### A.14. More real-world visual deraining results by training real-world rainy images

Training and testing on real-world rainy images can verify the representation ability of the model in the real world. In Section 4.2, we use the real-world dataset SPA-Data to train FourierMamba and report quantitative results. In this section, we show the visualization results of training and testing using SPA-Data, as shown in Figure 16. It can be seen that our method excels at removing rain and recovering details to obtain pleasing visual results. In addition, we also train and test FourierMamba on RainDS-Real (Quan et al., 2021) to further verify its effectiveness in real-world scenes. As shown in Table 14, our method can still achieve excellent performance.

### A.15. Metrics that can better reflect human perceptions

In this section, we use some metrics that better reflect human perception to evaluate our method. We use the more widely used perceptual metrics BRISQUE (Mittal et al., 2012b), NIQE (Mittal et al., 2012a), SSEQ (Liu et al., 2014), as shown in Table 15. It can be seen that our method can also achieve excellent performance on perceptual metrics.

Table 13. Quantitative results of testing on the real-world dataset RainDS-Real (Quan et al., 2021).

Method	PReNet	RESCAN	Restormer	HiNet	MSPFN	MPRNet	Ours
PSNR	24.15	24.29	24.54	24.71	24.76	25.07	<b>25.12</b>
SSIM	0.711	0.717	0.727	0.9731	0.729	0.736	<b>0.738</b>



Figure 10. Qualitative comparison on Rain100L (Yang et al., 2017). Zoom in for better visualization.



Figure 11. Qualitative comparison on Test2800 (Fu et al., 2017b). Zoom in for better visualization.

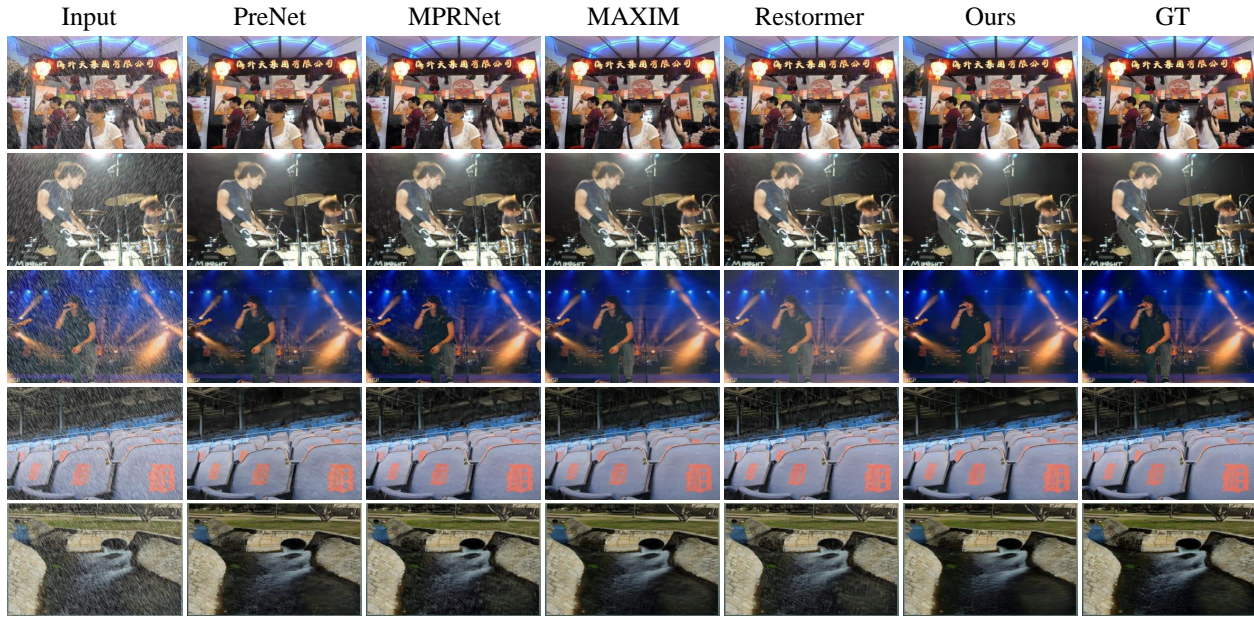


Figure 12. Qualitative comparison on Test1200 (Zhang & Patel, 2018). Zoom in for better visualization.

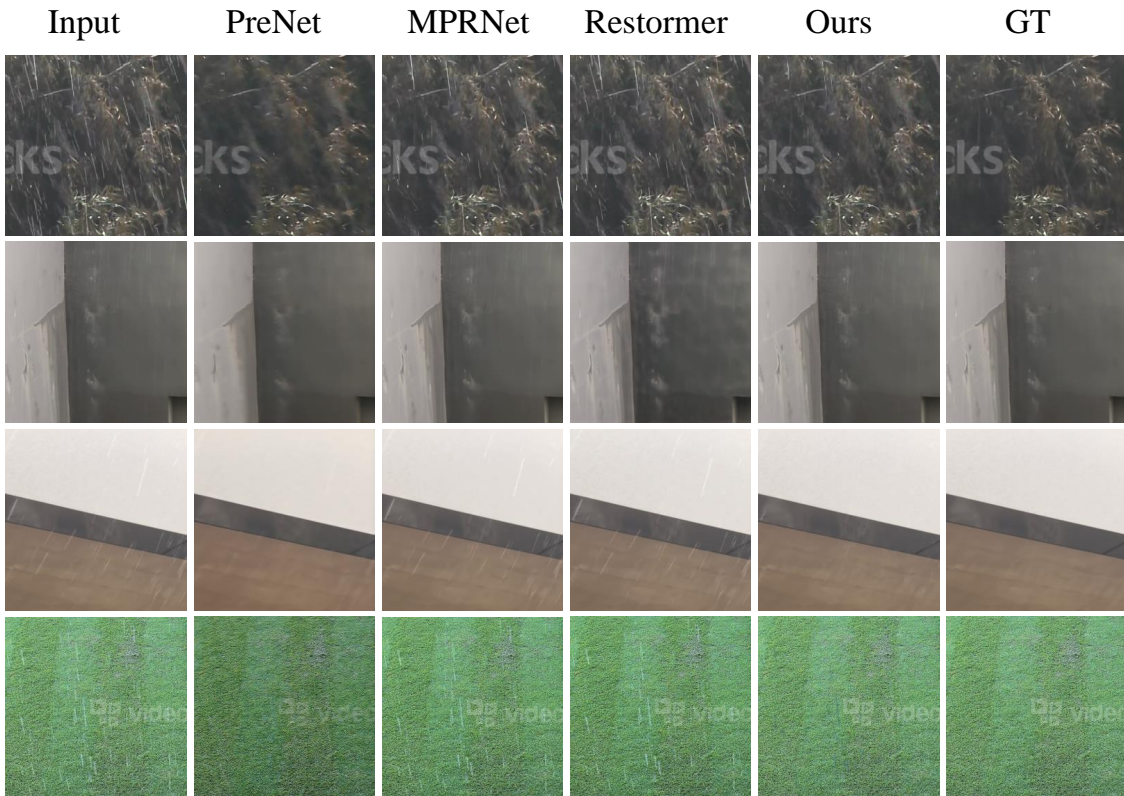


Figure 13. Qualitative comparison of real-world rainy images from SPA-Data(Wang et al., 2019).

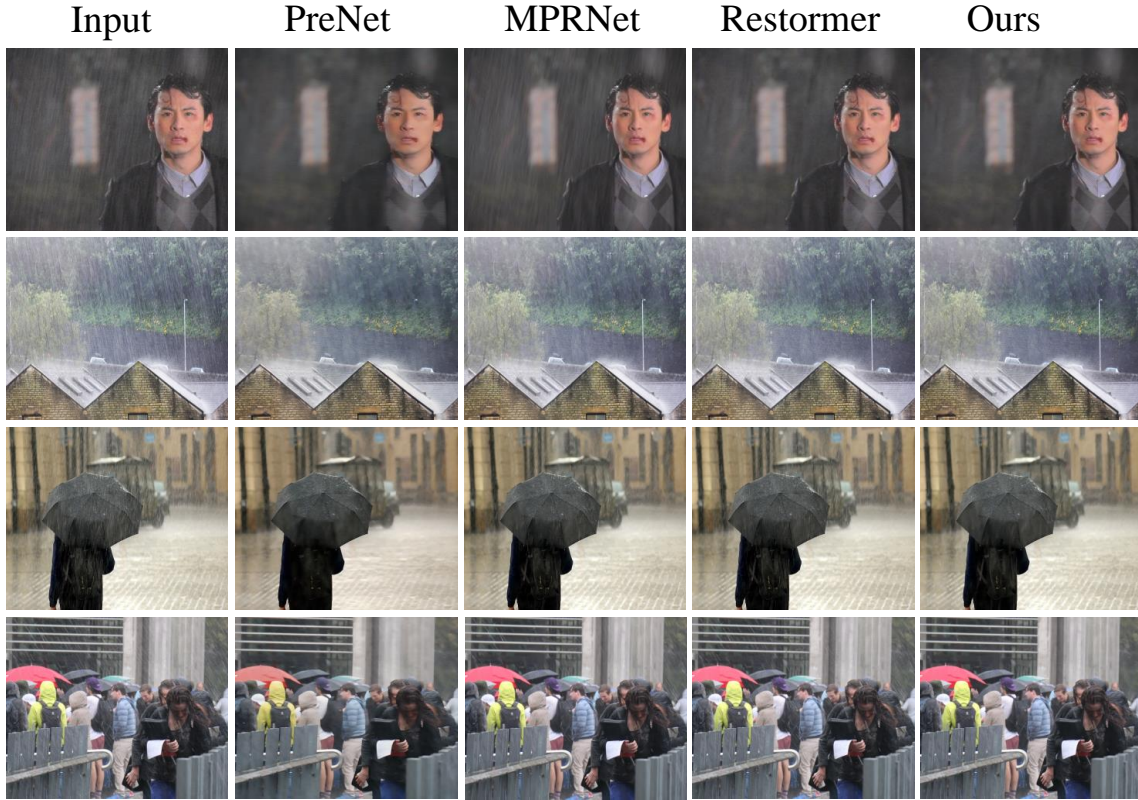


Figure 14. Qualitative comparison of real-world rainy images from RE-RAIN (Chen et al., 2023b).

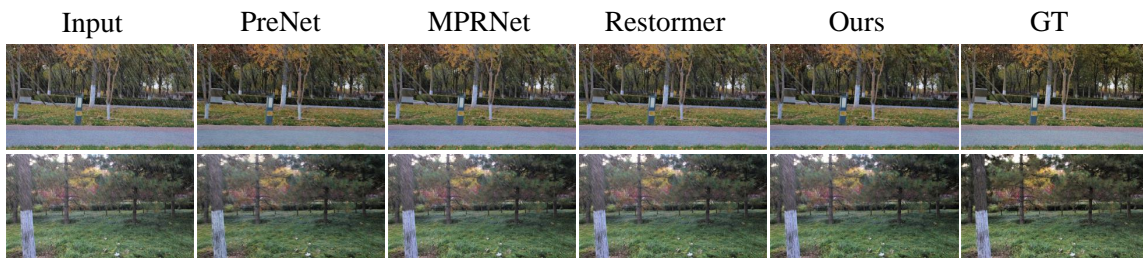


Figure 15. Qualitative results of real-world rainy images from RainDS-Real. (Quan et al., 2021).

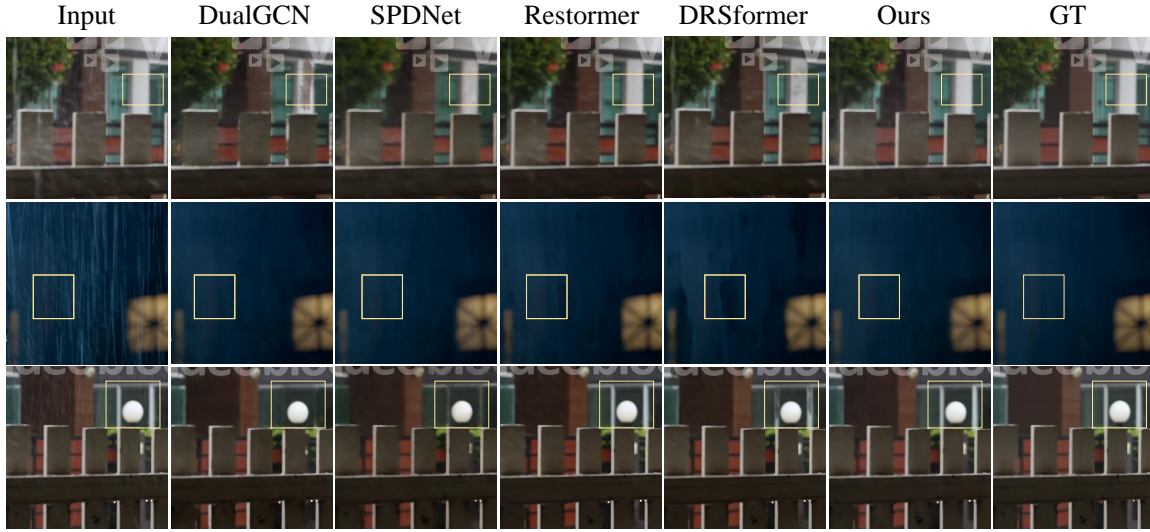


Figure 16. Qualitative results of training and testing on SPA-Data. (Wang et al., 2019).

Table 14. Quantitative comparison of training and testing on the real-world dataset RainDS-Real.

Method	PReNet	MSPFN	RCDNet	MPRNet	SwinIR	Restormer	Ours
PSNR	26.43	26.45	26.71	27.51	27.53	27.57	<b>27.69</b>
SSIM	0.7294	0.7270	0.7180	0.7355	0.7425	0.7438	<b>0.7482</b>

### A.16. More about the Optimization

In the main body, we describe that apply the L1 loss based on the Fourier transform. Here, we introduce the loss function in the frequency domain in further detail. we first use the Fourier transform to convert  $Y_{out}$  and  $Y_{gt}$  into the Fourier space. Then, the  $\mathcal{L}_1$ -norm of the amplitude difference and phase difference between  $Y_{out}$  and  $Y_{gt}$  are calculated and summed to produce the total frequency loss as following:

$$\|\mathcal{F}(Y_{out}) - \mathcal{F}(Y_{gt})\|_1 = \|\mathcal{A}(Y_{out}) - \mathcal{A}(Y_{gt})\|_1 + \|\mathcal{P}(Y_{out}) - \mathcal{P}(Y_{gt})\|_1. \quad (15)$$

### A.17. Ablation study on different frequency domain loss functions

We use three additional frequency domain loss functions: Phase Consistency Loss (PCL), Frequency Distribution Loss (FDL), and Focal Frequency Loss (FFL) (Jiang et al., 2021) for comparison with the L1 frequency domain loss we use. PCL is defined as the mean squared error of the phase difference between two images in the frequency domain, expressed as:

$$\mathcal{L}_{PCL} = \frac{1}{HW} \sum_{u,v} |\mathcal{P}(Y_{out})(u,v) - \mathcal{P}(Y_{gt})(u,v)|^2. \quad (16)$$

FDL represents the difference in frequency domain amplitude distributions between two images, expressed as:

$$\mathcal{L}_{FDL} = \frac{1}{HW} \sum_{u,v} |\mathcal{A}(Y_{out})(u,v) - \mathcal{A}(Y_{gt})(u,v)|^2. \quad (17)$$

FFL focuses on frequency components that are difficult to synthesize by down-weighting the easier ones, expressed as:

$$w(u,v) = |\mathcal{F}(Y_{out})(u,v) - \mathcal{F}(Y_{gt})(u,v)|^\alpha, \\ \mathcal{L}_{FFL} = \frac{1}{HW} \sum_{u=0}^{H-1} \sum_{v=0}^{W-1} w(u,v) |\mathcal{F}(Y_{out})(u,v) - \mathcal{F}(Y_{gt})(u,v)|^2, \quad (18)$$

where  $\mathcal{F}(\cdot)(u,v)$  represents the Fourier Transform,  $w(u,v)$  is the weight for the spatial frequency at  $(u,v)$ , and  $\alpha$  is the scaling factor for flexibility ( $\alpha = 1$  in practice).

**Table 15.** Performance comparison of different methods on various datasets. Metrics include BRISQUE, NIQE, and SSEQ.

Dataset Method	Rain100L			Rain100H			Test2800			Test1200			Test100		
	BRISQUE ↓	NIQE ↓	SSEQ ↓	BRISQUE ↓	NIQE ↓	SSEQ ↓	BRISQUE ↓	NIQE ↓	SSEQ ↓	BRISQUE ↓	NIQE ↓	SSEQ ↓	BRISQUE ↓	NIQE ↓	SSEQ ↓
MPRNet	17.791	6.816	12.702	16.287	6.973	13.860	15.782	6.251	9.470	23.434	5.742	12.653	23.526	6.903	12.767
MAXIM	<b>11.960</b>	<b>6.402</b>	<b>9.658</b>	14.622	6.929	8.034	15.272	6.114	8.760	25.026	5.573	14.760	22.433	6.770	12.615
Restormer	16.253	6.555	11.480	17.606	6.843	13.953	18.601	6.169	9.579	25.507	<b>5.534</b>	16.121	23.937	7.024	14.382
MambalIR	15.662	6.553	11.527	<b>10.350</b>	6.104	8.719	<u>13.246</u>	6.165	8.332	<b>20.743</b>	5.570	10.877	17.886	5.969	8.390
VmambalIR	16.073	6.651	11.061	11.686	<b>5.713</b>	8.302	13.465	6.114	<b>8.306</b>	<u>20.851</u>	5.553	<b>10.610</b>	<u>17.805</u>	<b>5.751</b>	8.548
FreqMamba	14.894	6.465	10.286	15.151	<b>5.450</b>	<b>4.704</b>	19.942	5.439	10.371	22.132	5.785	10.742	18.934	<b>5.898</b>	<u>7.247</u>
Ours	12.178	<b>6.261</b>	<u>10.008</u>	<u>10.607</u>	6.009	<u>5.826</u>	<b>12.895</b>	<b>5.258</b>	<b>8.286</b>	21.467	<u>5.538</u>	10.839	<b>17.738</b>	<u>5.958</u>	<b>7.102</b>

We conduct ablation comparison experiments on these loss functions, as shown in Table 16. It can be seen that the performance obtained by these four loss functions is similar. The focus of this work is on the design of the network architecture, so we follow existing methods (Zhou et al., 2023; Zhen et al., 2024) to use the L1 norm in the frequency domain. We will explore more frequency-domain loss functions in future work.

**Table 16.** Comparison results of different frequency-domain loss functions.

	PCL	FDL	FFL	Ours
PSNR	39.67	39.69	39.75	39.73
SSIM	0.9848	0.9852	0.9859	0.9856

### A.18. More visualizations for ablation studies

In Section 4.3, we perform ablation studies on the key designs and scanning methods of the proposed method. To further verify the effectiveness of the proposed method, we provide visualizations of the above ablation studies. Specifically, we subtract the restored images obtained from each ablation study from the ground truth to show the effect of each design. Figure 17 shows the visualization of the ablation study in Table 3. It can be seen that all designs have a significant effect on rain removal. Figure 18 shows the visualization of the ablation study of various scanning methods in Table 4. Both Figures 4 and Figures 18 illustrate that orderly correlation of different frequencies can promote rain removal.

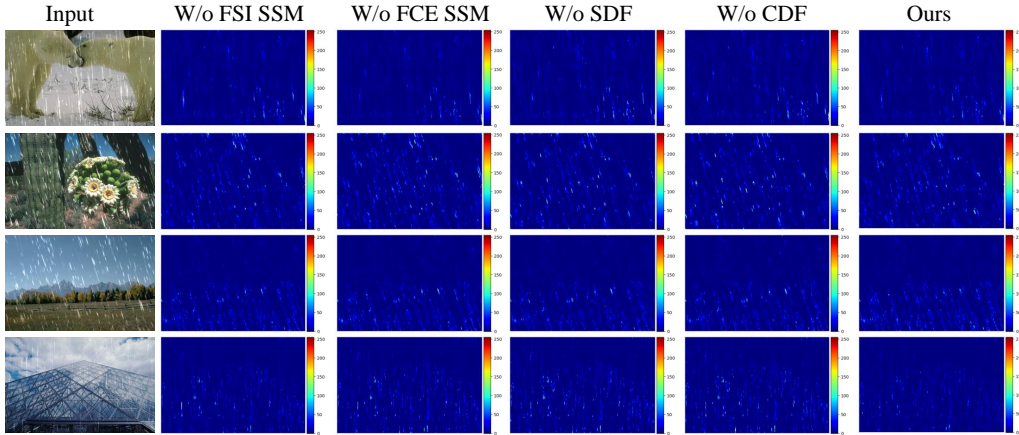


**Figure 17.** Visualization of ablation studies of various key designs of the proposed method.

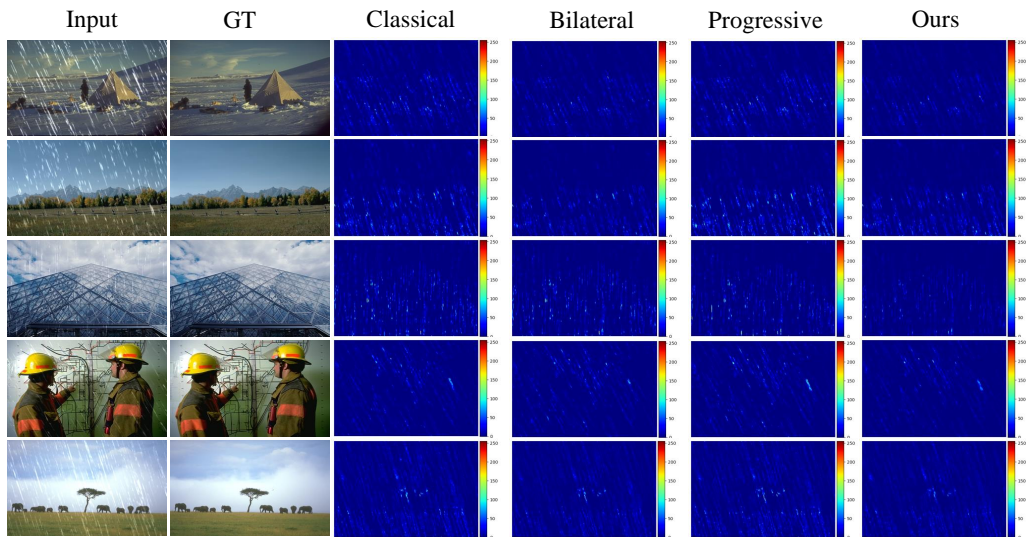


*Figure 18.* Visualization of ablation studies of different scanning methods in Fourier space.